ELSEVIER

Nuclear Physics A 633 (1998) 565–612

NUCLEAR PHYSICS A

Prolate–oblate shape coexistence in ^{75}Kr

S. Skoda [a], F. Becker [a], T. Burkardt [a], J. Eberth [a], S. Freund [a], U. Hermkens [a], T. Mylaeus [a], R. Sefzig [a], W. Teichert [a], A. von der Werth [a], H. Grawe [b], A. Kuhnert [b], K.H. Maier [b], J. Bea [c], B. Rubio [c]

[a] *Institute for Nuclear Physics, University of Cologne, Zülpicher Str. 77, D-50937 Cologne, Germany*
[b] *Hahn-Meitner-Institut, sector P, Glienicker Straße, D-14109 Berlin, Germany*
[c] *Instituto de Fisica corpuscular, Avda. Dr. Moliner 50, E-46100 Burjassot (Valencia), Spain*

Received 3 June 1996; revised 10 October 1997; accepted 19 November 1997

Abstract

The collective bands of ^{75}Kr were extended up to spin 45/2 using the compound reactions ^{50}Cr(^{28}Si,2pn), ^{54}Fe(^{24}Mg,2pn) and ^{58}Ni(^{20}Ne,2pn)^{75}Kr. Lifetimes were measured by RDDS with nine OSIRIS detectors in coincidence. Mixing ratios were determined by measurements of internal conversion coefficients, angular distribution and correlations. Deviations between different measurements are explained by the short lifetimes leading to angle dependent intensity losses due to Doppler shift. Spins and parities were assigned from angular distributions, excitation functions and DCO ratios measured with the OSIRIS_12 spectrometer. The band head spin of the negative parity yrast band was established as 3/2 via DCO ratios and internal conversion coefficients. Further bands at low excitation energy were found. In accordance to Woods–Saxon cranking model calculations, these weaker populated sidebands are interpreted to be built on oblate deformed intrinsic states ($\beta_2 \approx -0.2$), while the strongly populated bands are built on prolate deformed states ($\beta_2 \approx +0.4$). The interpretation of the 1qp $g_{9/2}$ yrare band, to be generated from oblate deformation, is further supported by $\Delta I = 0$ transitions into the yrast band and a similar oblate deformed $g_{9/2}$ structure in the isotone ^{73}Se. The experimental level energies, branching ratios, transition probabilities and mixing ratios are compared to rotor model calculations. The deviations between experiment and rotor model calculations are interpreted to be based on mixing between prolate and oblate states. © 1998 Elsevier Science B.V.

PACS: 21.10.-k; 21.10.Hw; 21.10.Ky; 21.10.Re; 21.10.Tg; 21.60.Ev; 23.20.-g; 23.20.En; 23.20.Gq; 23.20.Lv; 23.20.Nx; 25.70.Gh

Keywords: NUCLEAR REACTIONS ^{50}Cr(^{28}Si,n2p) $E = 95$ MeV; ^{54}Fe(^{24}Mg,n2p), $E = 75, 80$ MeV; ^{58}Ni(^{20}Ne,n2p), $E = 80, 84$ MeV; Measured $\sigma(E_\gamma, \theta)$, I_γ, $\gamma\gamma$-coin, I(ce). ^{75}Kr deduced high-spin levels, J, π, ICC, quadrupole moment, B(E2), B(M1), $T_{1/2}$.

PII S0375-9474(98)00644-1

1. Introduction

Neutron deficient nuclei with $A \approx 70-80$ and $N \approx Z$ show many fascinating features. Very different shapes are possible and a single nucleus may even exhibit quite different shapes at low excitation energies.

This so called shape-coexistence effect and the strong shape variation as a function of particle number, excitation energy and spin may be interpreted as resulting either from stabilizing energy gaps between the single-particle states at large deformation [1], or from the proton–neutron interaction and varying numbers of active nucleons resulting from sub-shells and full shell valence spaces [2,3].

The first example of shape coexistence in the mass region $A \approx 70-80$ was found in ^{72}Se [4]. Bengtsson et al. [5], confirmed by Nazarewicz et al. [1], calculated for $_{36}$Kr and $_{38}$Sr ($N \leqslant 40$) competing minima at quadrupole deformations $\beta_2 \approx +0.38$ (prolate) and $\beta_2 \approx -0.30$ (oblate). In agreement with these calculations, we found in ^{69,71}Se clear experimental evidence for collective oblate deformation [6]. These results strongly support the interpretation of the level structure of the neighboring even–even nuclei ^{70,72}Se [4,7] and ^{74,76}Kr [8–10]. Their low spin ($I \leqslant 8$) level structure is dominated by shape coexistence and mixing between prolate and oblate states.

We recently identified ^{73}Kr and established a level scheme for ^{73}Kr [11]. The negative parity band is built on the $3/2^-$-ground state (spin fixed by [12]) with large prolate deformation while the level structure above the $g_{9/2}$ isomer might originate from oblate deformation. In contradiction to model calculations of Bengtsson et al. [5] and Nazarewicz et al. [1] a large oblate ground-state deformation could not be established.

The nucleus ^{75}Kr has been studied by Winter et al., Garcia Bermudez et al., Herath-Banda et al., Chishti et al., Winchell et al., Cardona et al., and by our group [13–19]. Our recent results complement the work done before.

The $\gamma\gamma$-coincidences were measured with a thick target (Section 2.1) and a thin target (Section 2.2). Both coincidence measurements yielded transition intensities (Section 2.3). Spins were determined by ratios of Directional Correlations of two γ-rays emitted by an Oriented source (DCO) (Section 2.4). Mixing ratios δ(E2/M1), crucial for the determination of $B(\mathrm{E2}, \Delta I = 1)$-values, were evaluated by measuring internal conversion probabilities (Section 2.5). From $\gamma\gamma$-coincidences, intensities and DCO-ratios an extended level scheme was built up to spin 45/2, which includes low spin off-yrast levels at low excitation energy arranged in band structures (Section 2.6). Further, to compare experimental values with model calculations we measured picosecond lifetimes in coincidence (Section 2.7).

The nucleus ^{75}Kr appears to have a large prolate deformation, which is reproduced by Woods–Saxon cranking calculations (Section 3.1), because the level energies and $B(\mathrm{E2}, \Delta I = 2)$ transition probabilities can be reproduced by model calculations using large prolate deformations for both yrast bands (Section 3.2). The relations between intensities and mixing ratios, given by angular distributions and conversion coefficients, are compared to rotor calculations (Section 3.2). In our previous investigation of ^{75}Kr we found inconsistencies between the level scheme, which appears to represent a strong

coupling scheme with large prolate deformation, and the electro-magnetic decay properties, which hint on prolate-oblate shape mixing. This subject will be discussed in Section 3.3.

2. Experimental methods and results

The experiments were performed with 95 MeV ^{28}Si and 75,80 MeV ^{24}Mg beams from the HVEC FN tandem accelerator of the University of Cologne and with an 80 MeV ^{20}Ne beam provided by VICKSI of the Hahn-Meitner-Institute in Berlin. High spin states in ^{75}Kr were populated via the reactions ^{50}Cr(^{28}Si,2pn), ^{54}Fe(^{24}Mg,2pn) and ^{58}Ni(^{20}Ne,2pn)^{75}Kr. In all reactions ^{75}Kr was produced with 20–30% of the total cross section. Enriched targets, several 100 μg/cm^2 thick, were used. The ^{50}Cr target (96.4%, 300 μg/cm^2) was sputtered and the ^{58}Ni target (99.9%, 1 mg/cm^2) was rolled onto the beam stopper, a bismuth–indium–copper sandwich [20]; the ^{54}Fe target (94.3%, 450 μg/cm^2) used in the recoil-distance Doppler-shift measurement was rolled as was the ^{181}Ta recoil stopper foil. The enriched ^{54}Fe target (94.3%, 800 μg/cm^2), used in the internal conversion measurement, was rolled. Further, 1.5–2 mg/cm^2 ^{12}C was evaporated onto the Fe foil to stop the recoiling nuclei. Nuclei of the ^{24}Mg+^{12}C reaction decay in flight, therefore their transitions only produce an enhanced background.

For the data analysis a number of computer codes developed at the University of Cologne were used subject to the quantities to be analysed ([21–23]).

2.1. $\gamma\gamma$-coincidences measured with a thick target

The $\gamma\gamma$-coincidences were measured via the reaction ^{20}Ne+^{58}Ni at a beam energy of 80 MeV with the OSIRIS spectrometer. The OSIRIS spectrometer consists of twelve detectors, each consisting of a Ge detector of about 25–28% efficiency surrounded by a BGO escape suppression shield [24]. The OSIRIS_12 spectrometer was used in a ring configuration mounted parallel to the beam. The detectors were positioned at the angles 25°, 38°, 63°, 90°, 117°, 142° and 155° (see also Fig. 1 in Ref. [19]). The coincidence events were recorded in list mode and stored on magnetic tape. Various matrices were constructed off-line to study $\gamma\gamma$ coincidence relationships and *D*irectional *C*orrelations of two γ-rays emitted by an *O*riented source (DCO) for spin determination (see Section 2.4). The new transitions in ^{75}Kr were obtained from the symmetrical sum matrix gained from the 66 possible detector combinations in the twelve detector measurement (123×10^6 events).

The twelve-detector experiment was designed to search for weakly populated off-yrast levels at low excitation energy in ^{75}Kr. This goal has been achieved. Fig. 1 shows spectra gated by two transitions which have been resolved in this measurement as doublets in ^{75}Kr (749,752 and 852,854 keV). Thus, the level scheme had to be rearranged in a new pattern compared to Ref. [19]. Despite some ambiguities, e.g in the excitation functions [25], in the old level scheme the feeding point of the 750–577–608 keV

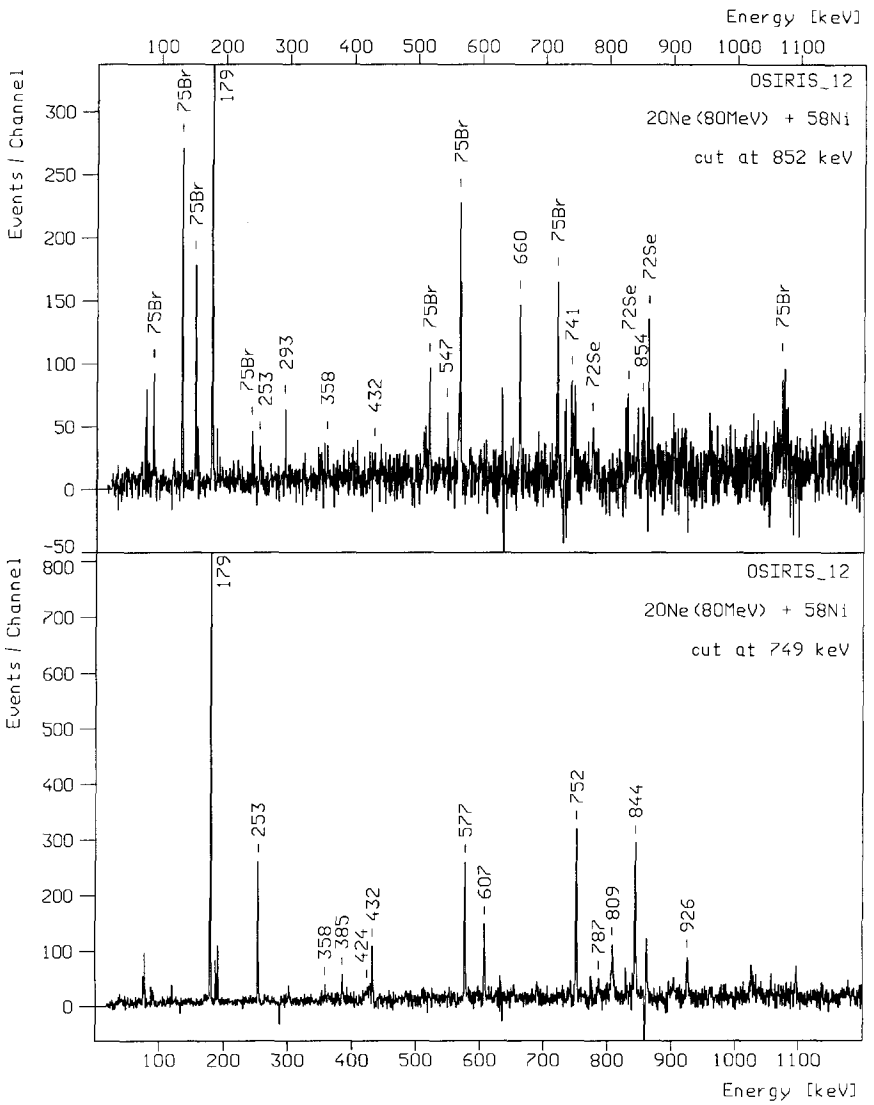

Fig. 1. Resolved doublets of the coincident transitions 852, 854 keV and 749, 752 keV presented in spectra gated by the respectively stronger transition. All four transitions populate the main negative parity band from the side. Contaminations are indicated by their origin.

coincidences had been defined by the 844 keV yrast band transition, which now has been identified as a doublet in ^{75}Kr. Likewise the feeding point of other transitions had been defined in Ref. [19] by the yrast band transition with the highest excitation energy observed in coincidence.

The OSIRIS spectrometer had been combined with an inner shell of 48 BGO detectors providing a sum energy and multiplicity filter. Fig. 2 shows the sum energy and multiplicity distribution for various channels of the ^{20}Ne+^{58}Ni reaction. Since ^{75}Kr has many transition energies in common with ^{73,74}Br and other lighter nuclei, a lower threshold

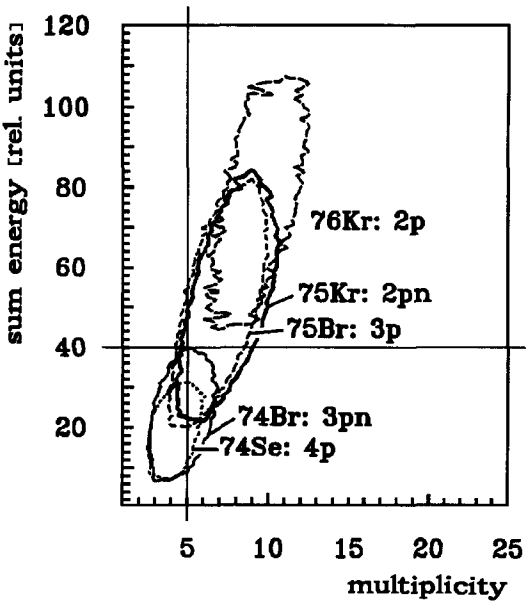

Fig. 2. Distribution of sum energy and multiplicity measured with a 48 BGO ball for various reaction channels of the reaction ^{58}Ni(^{20}Ne, X)Y at 80 MeV beam energy. Gating on strong and pure γ transitions yields characteristic distributions in the (sum energy, multiplicity) matrix. Lighter residual nuclei can be suppressed when sum energy and multiplicity are required to exceed certain values indicated by the straight lines.

was set on the sum energy and the multiplicity values to separate the heavier nuclei from the lighter. Thus, it was moreover possible to check that the intensity of transitions newly attributed to ^{75}Kr as well as the intensity of already adopted ^{75}Kr transitions is better conserved by the additional (sum energy, multiplicity)-condition than for the suppressed channels. An example for a newly identified transition is shown in Fig. 3 (1150 keV).

2.2. *Coincidences measured with a thin target*

A plunger measurement was performed with five OSIRIS detectors at 143° and four OSIRIS detectors at 41°, arranged around the beam axis on a forward and backward cone pointing at the target. The $\gamma\gamma$-coincidence experiment was designed to study lifetimes in the ps range with the Recoil Distance Doppler Shift method (RDDS) (see also Section 2.7). The coincidence events were recorded in list mode and stored on magnetic tape. Matrices were constructed off-line to study stop and flight peak intensities for six different distances and the four possible angular combinations. The coincidence matrices gained for the six different distances were added. Levels with lifetimes less than 0.5 ps decayed predominantly in flight. Thus, for the high spin transitions in ^{75}Kr all intensity was concentrated in the flight peaks in contrast to the thick target measurement where the intensity was smeared out over several 10 keV due to Doppler Shift Attenuation (DSA)

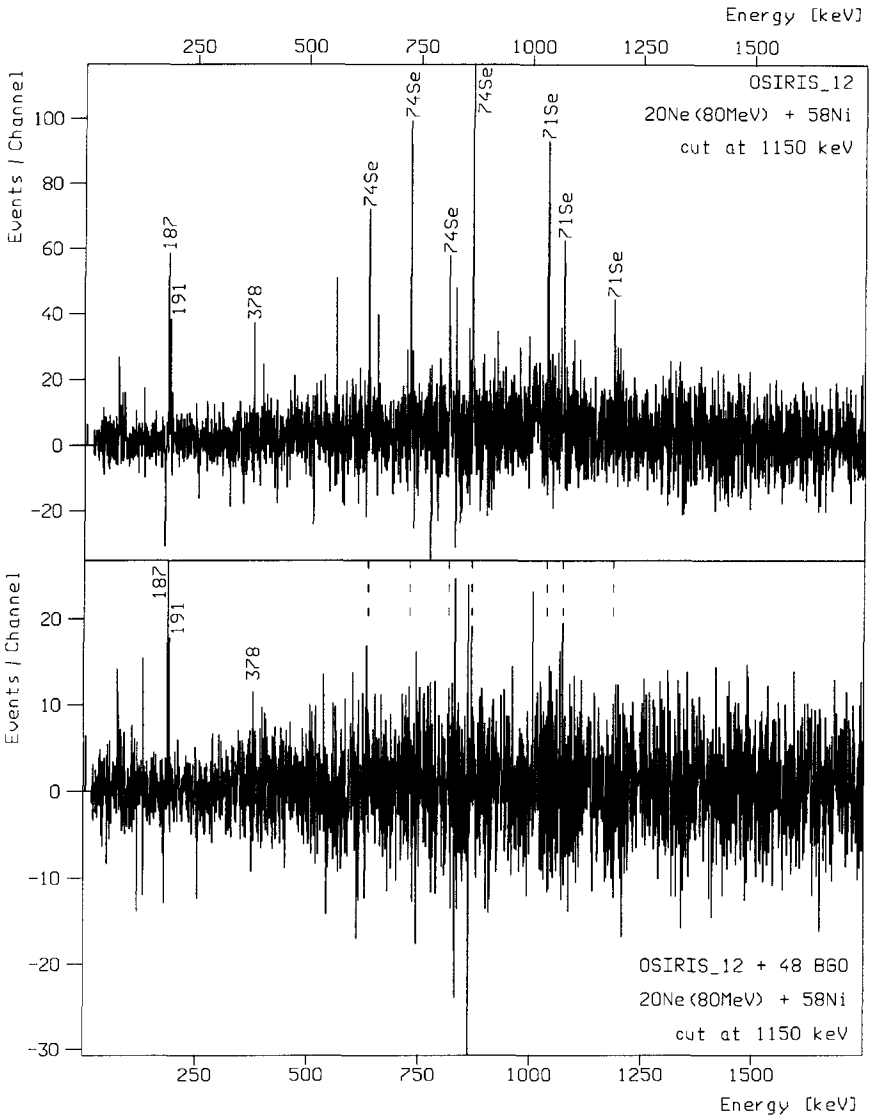

Fig. 3. Comparison of a spectrum gated by the 1150 keV transition, populating the positive parity band from the side, without (top) and with (bottom) restrictions on the sum energy and multiplicity values. In case of the lower spectrum sum energy and multiplicity are required to exceed the values marked in Fig. 2. The lighter residual nuclei ^{71,74}Se are obviously more suppressed.

in the thick target and the multitude of detector angles. The 143°–41° (21×10^6 events) and the 143°–143° matrices (10×10^6 events) were studied. No further information could be obtained from the 41°–41° matrix (6×10^6 events). As an example for the data quality in the OSIRIS_12 and OSIRIS_9 coincidence measurements the spectra gated by the 253 keV line are compared in Fig. 4.

Our data confirm the measurements of Chishti et al. as well as of Winchell et

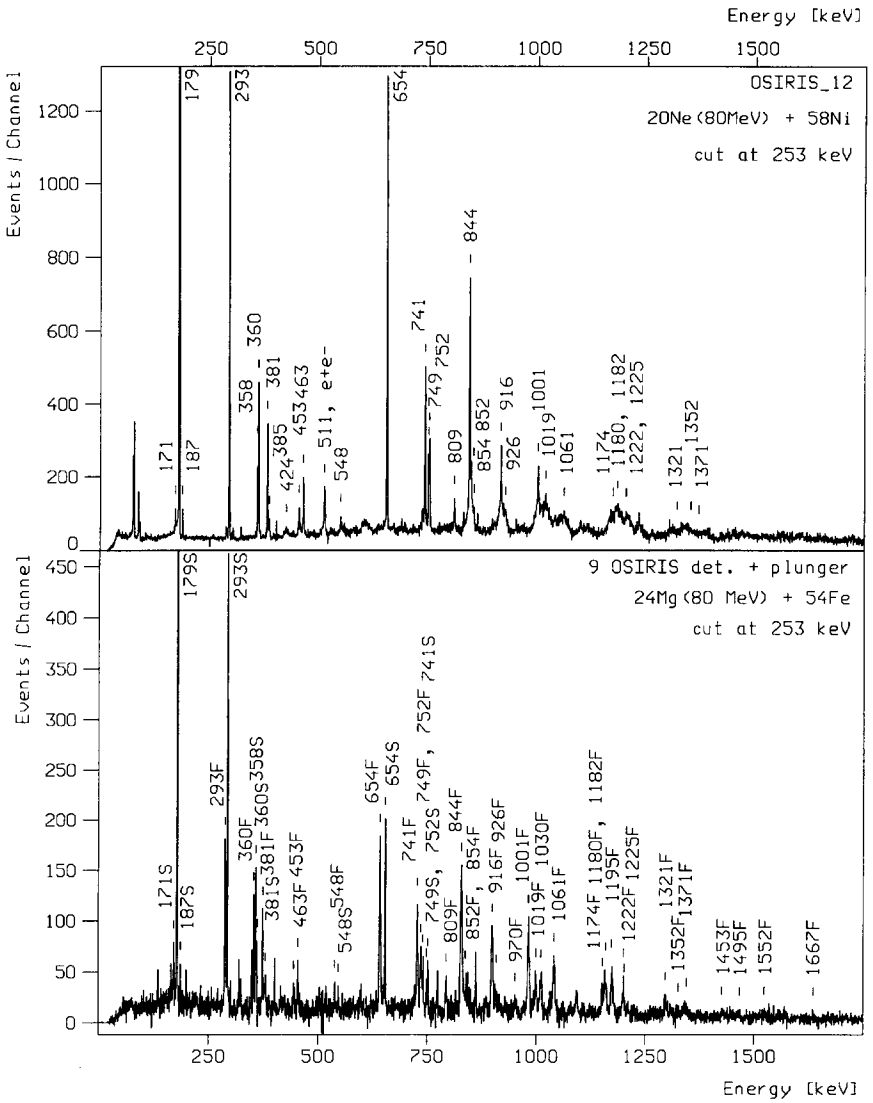

Fig. 4. Comparison of a measurement with thick target and various observation angles from 25° up to 155° (top) and a measurement with thin target and observation angle 143° (bottom). All lines marked by their transition energy are assigned to ^{75}Kr. Bottom: stop peaks are marked by S and flight peaks are indicated by F.

al. ([16,17]) and extend the level scheme further. Especially, a forking in the negative parity band was found which explains the disagreement between the works of Chishti et al. and Winchell et al. ([16,17]). Moreover, together with the thick target measurement (Section 2.1) we established additional low spin levels at low excitation energy arranged in band structures feeding into the yrast bands of the respective same parity.

Table 1
Comparison of branching ratios in different experiments.
The errors take into account the error of the individual as well as of the added intensities. $\lambda = \frac{\text{Int.}_\gamma(I \to I-2)}{\text{Int.}_\gamma(I \to I-1)}$

	Spin	E_x	E_γ	Branching B (%)						
		(keV)	(keV)	OSIRIS_12	OSIRIS_9	[16]	[17]	[18]	$\langle B \rangle$	λ
$\pi = +$	9/2	378	378	26(1)		29(2)	24(4)	26(3)	27(1)	
			191	74(2)		71(3)	76(12)	74(9)	73(2)	0.37(2)
	11/2	770	583	38(2)		45(2)	30(5)	42(7)	41(1)	
			392	62(3)		55(3)	70(10)	58(10)	59(2)	0.69(3)
	13/2	1067	689	74(4)		75(4)	66(9)	70(14)	74(3)	
			297	26(2)		25(2)	34(5)	30(6)	26(1)	2.8(2)
	15/2	1594	824	58(5)	62(13)	58(4)	50(10)		58(3)	
			527	42(4)	38(8)	42(3)	50(10)		42(2)	1.4(1)
	17/2	1963	896	83(12)	86(12)	87(5)	83(27)		86(4)	
			370	17(3)	14(2)	13(2)	17(6)		14(1)	6.1(5)
	19/2	2629	1035		73(10)	76(6)	43(14)		73(6)	
			665		27(4)	24(4)	57(18)		27(3)	2.7(4)
$\pi = -$	7/2	611	432	25(1)		28(2)	29(4)	28(5)	26(1)	
			253	73(3)		72(2)	71(10)	72(12)	72(2)	0.36(2)
			234	2(1)					2(1)	
	9/2	904	547	48(2)		47(4)	45(6)	50(12)	48(2)	
			293	52(2)		53(3)	55(7)	50(12)	52(2)	0.92(5)
	11/2	1264	654	56(5)	62(7)	63(4)	61(4)	58(16)	61(3)	
			360	44(4)	38(4)	37(2)	39(9)	42(11)	39(2)	1.6(1)
	13/2	1645	741	70(8)	71(10)	64(4)	71(14)		67(3)	
			381	30(4)	29(4)	36(3)	29(6)		33(2)	2.0(2)
	15/2	2108	844	81(17)	81(7)	85(5)	82(26)		83(4)	
			463	19(4)	19(2)	15(2)	18(6)		17(1)	4.9(4)
	17/2	2562	916		89(12)	88(6)	74(23)		88(5)	
			453		11(2)	12(3)	26(8)		12(2)	7.3(1)

2.3. Intensities

The branching ratios for the yrast transitions up to spin $17/2^+$ and $11/2^-$ were determined from spectra gated by their direct feeders in the symmetric OSIRIS_12 matrix. A slight enhancement of the yield of E2-transitions due to the mean detector angle 52.8° was taken into account. The branching ratios determined from the OSIRIS_12 and the OSIRIS_9 measurement, listed in Table 1, compare well with one another and also with previously published data.

The relative intensities were determined from spectra of which the gates were set on low spin transitions in the (41° gate, 143° spectrum) matrix from the OSIRIS_9 lifetime measurement. Based upon the use of only one observation angle and a thin target, the transition intensity is concentrated in a stop and flight peak in contrast to the OSIRIS_12 measurement (see also Section 2.2).

The angular correlations in the OSIRIS_9 measurement were taken into account as follows. The $\Delta I = 1$ transitions feeding into the $5/2^+$ band were normalized to the

392 keV intensity determined in the neutron coincident angular distribution published in Ref. [19]. The 297/689 branching ratio was taken from Table 1 and all E2 transitions feeding into the $5/2^+$ band were normalized to the calculated intensity of the 689 keV transition. For the transitions feeding into the $3/2^-$ band, ΔI=1 transitions were normalized to the 253 keV transition intensity and the E2 transitions were normalized to the 547 keV transitions intensity, either measured via neutron coincident angular distribution [19].

The relative intensities, measured with OSIRIS_9, are listed in Table 2. Intensities of weak negative parity sideband transitions could be determined only in the OSIRIS_12 matrix. Additionally, the OSIRIS_12 intensities for high spin transitions from negative parity states are included for comparison. Due to Doppler shift the transition intensity is spread with increasing spin over more and more channels, which made the intensity determination increasingly difficult. The resulting intensity loss is evident when compared to the OSIRIS_9 intensities.

2.4. DCO ratios

To gain information about spin differences DCO ratios were analyzed in OSIRIS_12 matrices. The DCO ratio was defined as

$$R_{\mathrm{DCO}} = \frac{\text{Yield (gated by } \gamma_1 \text{ at } \Theta_1,\ \gamma_2 \text{ observed at } \Theta_2)}{\text{Yield (gated by } \gamma_1 \text{ at } 25°,\ \gamma_2 \text{ observed at } 90°)}\,. \tag{1}$$

Thus, to be independent of absolute values, each DCO value is compared to the (25°, 90°) DCO value. Spins were determined via DCO ratios for the (90°, 25°) detector combination, mixing ratios were determined by using likewise the combinations (38°, 25°) and (25°, 38°). The DCO ratios were corrected for efficiency differences. The time window was about 200 ns. Therefore, low energy signals maintained full line intensity albeit late constant fraction triggering due to smaller leading edge slopes.

For transitions of known multipolarity the DCO ratios of the (90°, 25°) combination were evaluated to obtain a standard. As expected, (ΔI = 2 gate, ΔI = 2 spectrum) and (ΔI = 1, ΔI = 1) combinations gave R_{DCO} values around one, while (E2, ΔI = 1) combinations gave R_{DCO} values between 0.3 and 0.6 ($\approx$0.7 for stretched E1). Since ^{75}Kr has many strong ΔI = 1 transitions, ΔI = 1 transitions were also applied as gates, despite the variable mixing ratios δ. Nevertheless, $R_{\mathrm{DCO}}(\Delta I = 1, \Delta I = 1) \approx 1$ values are well separated from $R_{\mathrm{DCO}}(\Delta I = 1, \mathrm{E2}) \approx 2-4$ values, while (E1, E2) combinations only give $R_{\mathrm{DCO}} \approx 1-2$. The DCO ratios evaluated for ^{75}Kr were compared to the standard values shown in Fig. 5. Because of the various gating possibilities, many multi-polarities and hence spins could be determined, see Table 2.

Angular correlations were investigated concerning mixing ratios via the additional combinations (38°, 25°) and (25°, 38°), both were normalized to the (25°, 90°) DCO value (see also Ref. [23]). For the 432–179$_1$ keV coincidence the following values were determined: 0.68(5) for (90°, 25°), 0.92(7) for (38°, 25°) and 0.94(7) for (25°, 38°). From these values the following $(L+1)/L$ mixing ratios for the 179$_1$ keV

Table 2

Relative transition intensities and DCO ratios.

Relative Intensities, determined from the 143°–41° flight-time matrix (see Section 2.2), are given in the column labeled OSIRIS_9. Additionally, low spin negative parity sideband transition intensities were determined from the OSIRIS_12 experiment. Energy errors are about 0.3 keV (2 keV) for energies given with (without) decimal place. Spins in braces are restricted by DCO ratios. Spins in parentheses are proposed assuming E2 transitions of a rotational band. Based on comparisons to DCO ratios, measured with OSIRIS_12, for transitions of known characteristic (ΔI and $\Delta\pi$), shown in Fig. 5, transition characteristics are proposed for ^{75}Kr transitions. In most cases the unknown transition characteristic can be fixed due to the large amount of gating possibilities, of which only a few are presented here. $R_{DCO} = \frac{\text{Yield (gated by } \gamma_1 \text{ at } 90°, \gamma_2 \text{ observed at } 25°)}{\text{Yield (gated by } \gamma_1 \text{ at } 25°, \gamma_2 \text{ observed at } 90°)}$.

	E_x (keV)	Spin	E_γ (keV)	Relative intensity (%) OSIRIS_12	Relative intensity (%) OSIRIS_9	$R_{DCO}(\Delta R_{DCO})$	Transition	Gate	Assignment for E_γ
$\pi = +$	0	5/2							
	187.1	7/2	187.1		gate	0.37(2)	187	689	M1
	377.7	9/2	377.7		gate	0.93(9)	378	689	E2
			190.6		gate	0.37(2)	191	689	M1
	726.1	9/2	539.0		[a]	0.65(29)	539	187	
						0.62(9)	539	1051	$\Delta I = 0,1$;M1
			348.4		<1	0.89(17)	348	378	
						1.74(31)	348	191	$\Delta I = 0,2$
	769.8	11/2	582.7		70(3) [c]				
			392.1		100(4) [b]	0.36(3)	392	378	M1
	1067.1	13/2	689.4		184(9) [c]	1.00(7)	689	378	E2
			297.3		65(3)	0.41(6)	297	378	M1
	1527.8	13/2	1150.1		14(2)	1.23(23)	1150	378	E2
			801.6		<1	0.83(12)	802	1051	E2
	1593.5	15/2	823.7		65(8)	3.07(28)	824	392	E2
			526.5		39(7) [e],48(2) [d]	0.29(5)	527	689	M1
	1755.2	{11/2}	985.4		<1	0.75(18)	985	191	
						1.18(34)	985	378	$\Delta I = 0$
			1568.1		2(1) [a]				
	1963.3	17/2	896.2		145(17)	0.95(5)	896	689	E2
			369.8		23(1)	0.48(9)	370	378	M1

Table 2 — continued

	E_x (keV)	Spin	E_γ (keV)	Relative intensity (%) OSIRIS_12	Relative intensity (%) OSIRIS_9	$R_{DCO}(\Delta R_{DCO})$	Transition	Gate	Assignment for E_γ
$\pi = +$	2578.7	–	1511.6		7(2)				
			1050.9		14(2)	0.24(4)	191	1051	E2
	2628.8	19/2	1035.3		63(8)	1.30(21)	1035	378	E2
			665.4		23(1)	0.90(22)	665	187	M1
	2708.3	{15/2}	1938		<1				
			1114.8		13(2)	1.37(29)	1115	689	$\Delta I = 0,2$
			953		<1				
	3048.8	21/2	1085.5		112(14)	1.04(10)	1086	689	E2
			420.0		7(1)	0.83(16)	420	191	M1
	3464	–	1501		11(2)				
	3803.0	–	1094.7		10(2)				
	3823.7	23/2 [f]	1194.9		53(7)				
			774.9		13(1)				
	4277	25/2 [f]	1228		77(10)				
			453		4(1)				
	4647	–	1598		2(1)				
			1183		10(5) [D,e]				
	5025	(27/2)	1201		28(5)				
			748		15(1)				
	5558	29/2 [f]	1281		41(6)				
	(5971)	–	1324		11(2)				
	6309	(31/2)	1284		11(2)				
			752		10(1)				
	6891	(33/2)	1333		28(5)				
	(7507)	–	1536		10(5)				
	7842	(35/2)	1533		9(5)				
	8388	(37/2)	1497		20(3)				
	8920	–	532		9(5) [e,d]				
	(9323)	–	1816		9(5) [e],17(3) [D]				
	9452	(39/2)	1610		7(3)				

Table 2 — continued

	E_x (keV)	Spin	E_γ (keV)	Relative intensity (%) OSIRIS_12	Relative intensity (%) OSIRIS_9	$R_{DCO}(\Delta R_{DCO})$	Transition	Gate	Assignment for E_γ
$\pi = +$	10050	(41/2)	1662		12(2)				
	10490	–	1570		9(2)				
	11252	(43/2)	1800		7(2)				
	(11271)	–	1948		4(2)				
	11753	(45/2)	1703		5(2)				
	12284	–	1794		3(2)				
$\pi = -$	179.1 [h]	3/2	179.1 [h]	240(50) [e]	gate	0.67(4)	179_1	432	E1
	178.95(6) [i]		178.95(6) [i]						
	358.2 [h]	5/2	358.2	20(5)	*a*				
			179.1 [h]	220(40) [e]	gate				
	358.21(8) [i]		179.26(6) [i]						
			171.1	1(1) [e]	*a*	0.59(8)	171	654	
						2.34(28)	171	293	$\Delta I = 0,1,2$
	611.4	7/2	432.3	46(2) [c]	46(6) [c]	0.41(4)	293	432	E2
			253.3	126(2) [b]	126(2) [b]	0.39(2)	253	654	M1
			233.7	3(2) [c]	*a*	0.76(19)	234	654	
						0.92(26)	234	360	$\Delta I = 0,1$;E1
	786.6	5/2	607.4	17(5)	17(5)	0.45(5)	607	577	M1
			428.3	5(1)	4(1)				
	904.8	9/2	546.6	71(3) [b]	71(7) [b]				
			293.3	61(1)	61(2)	0.41(4)	293	432	M1
	1099.2	7/2	741.0	*D*	15(5) [e]	0.47(6)	741.0	660	M1
	1265.2	11/2	653.8	68(3)	68(7)				
			360.4	44(1)	42(1)	0.34(4)	360	547	M1
	1363.6	9/2	752.1	14(1)	19(4)	2.11(49)	432	752	
						1.13(10)	253	752	M1
			577.0	$\geqslant 11$	18(5) [e]	2.74(58)	577	607	
						1.32(25)	577	749	E2
	1645.9	13/2	741.0	*d*	62(8) [c]				
			380.8	23(1)	25(8)				

Table 2 — continued

	E_x (keV)	Spin	E_γ (keV)	Relative intensity (%) OSIRIS_12	Relative intensity (%) OSIRIS_9	$R_{DCO}(\Delta R_{DCO})$	Transition	Gate	Assignment for E_γ
$\pi = -$	1758.9	11/2	854.1	8(1)	*d*	2.17(96)	852	854	E2
			659.7	9(1)	14(2)	0.47(6)	741.0	660	
						0.64(7)	179[d]	660	E2
	2108.8	15/2	843.6	80(10)[e],100[d]	70(5)[e],100[d]				
			462.8	19(1)	17(1)				
	2112.9	13/2	847.7	9(1)	*d*	0.33(8)	848	654	M1
			749.3	19(1)	26(4)	1.35(13)	749	577	
						2.46(32)	749	607	E2
	2561.7	17/2	915.8	-	65(8)	1.32(13)	916	432+547	E2
			453.1	10(1)	8(1)				
	2610.9	15/2	852.0	7(1)	*d*	2.17(96)	852	854	
						1.37(18)	852	660	E2
	2956.9	17/2	844.0	20(10)[e],100[d]	30(5)[e],100[d]	2.21(49)	844.0	607	
						1.34(20)	844.0	577	E2
	3039.4	(17/2)	926.5	3(1)	6(6)				
	3109.9	19/2	1001.1	<87	52(5)	2.53(28)	1001	253+293	
						0.85(13)	1001	547	E2
			548.0	4(1)	10(5)				
	3341.8	(19/2)	1233.0	<25[d]	5(2)				
			385.0	4(1)	<1				
	3622.6	21/2	1060.9	<46	39(4)	1.05(14)	1061	432+547	E2
			512.8	*D*	*D*				
	3765.7	21/2	808.8	7(1)	16(2)	1.68(53)	809	577	E2
			423.8	4(1)	*d*				
	4128.7	23/2	1018.8	<49	32(3)	0.98(17)	1019	432+547	E2
			786.9	2(1)	<3				
			363.1	2(1)	*d*				
	4290	23/2[g]	1180	*d*	29(4)				
			667	*d*	*d*				

Table 2 — continued

	E_x (keV)	Spin	E_γ (keV)	Relative intensity (%) OSIRIS_12	Relative intensity (%) OSIRIS_9	$R_{DCO}(\Delta R_{DCO})$	Transition	Gate	Assignment for E_γ
$\pi = -$	4737	(25/2)	971	<1	8(2)				
			608	*d*	3(2) [e]				
	4817	(25/2)	1194	*d*	19(4)				
	5159	27/2	1030	<9	34(4)	0.93(19)	1030	547	E2
	5464	(27/2)	1174	*d*	20(5)				
	5919	(29/2)	1182	*d*	12(3)				
	6042	(29/2)	1225	*d*	11(2)				
	6357	(31/2)	1198	*d*	19(4)				
	6686	(31/2)	1222	*d*	15(3)				
	7240	(33/2)	1321		11(5) [e],<24 [D]				
	7728	(35/2)	1371		15(3)				
	8038	(35/2)	1352		8(2)				
	8694	(37/2)	1454		10(2)				
	9280	(39/2)	1552		7(2)				
	9529	(39/2)	1491		5(2)				
	11196	(43/2)	1667		4(1)				

Legend: a) those transitions are in parallel to the gating transitions, b) intensity fixed according to [19] (see text), c) intensity fixed by branching ratio, d) doublet in ^{75}Kr, D) doublet, e) estimated from feeding and depopulating intensities, f) spin fixed by Ref. [17], g) spin fixed because of strongly coupled band structure, h) measured in beam, i) measured with mass separator

Table 3

Mixing ratios deduced from various experiments.

Legend: E_γ = transition energy (keV), J_i = initial spin, Ref. = References: A = [14], B = [15], C = [19]: exp. with OSIRIS_10, D = [19]: exp. with turn table, E = this work, same data as in D, reanalyzed with XPLO [22]. A_k/A_0, α_k ($k = 2, 4$) and δ: experimental angular distribution coefficients with:

$$\delta = \frac{\langle J_f||L+1||J_i\rangle}{\langle J_f||L||J_i\rangle}$$

α_K: measured conversion probability

E_γ	$2J_i$	Ref.	A_2/A_0	A_4/A_0	α_2	α_4	α_K	δ	$+\Delta\delta$	$-\Delta\delta$	δ_{DCO}	$\delta_{adopted}$
$\pi = +, \Delta I = 1$												
187	7	B	−0.58(5)	0.16(5)	0.67(6)	0.28(9)		−2.06	0.08	0.23		
							0.034(2) [a]	±0.55	0.07	0.04		−0.55(6)
191	9	A	−0.47(4)	−0.02(2)								
		B	−0.60(5)	0.18(5)	0.75(6)	0.43(10)		−2.40	0.07	0.37		
		D	−0.52(2)	0.044(4)	0.46(2)	0.12(1)		−1.26	0.03	0.03		
											−0.22(8), −2.4(6)	
		E	−0.52(1)	0.05(1)	0.46(3)	0.12(2)		−1.2	0.3	0.2		
		E	−0.55(1)	0.06(1)	0.61(0)	0.22(0)		−0.29 [c]	0.01	0.01		
							0.033(3) [a]	±0.56	0.08	0.06		−0.56(7)
392	11	A	−0.69(5)	0.12(5)								
		B	−1.14(45)	0.62(34)	0.85(48)	0.80(74)		−1.90	0.55	1.82		
		C	−0.69(3)	0.06(1)	0.58(3)	0.20(2)		−1.04	0.13	0.13		
		D	−0.65(2)	0.052(4)	0.54(2)	0.17(1)		−1.01	0.03	0.03		
											−0.32(11), −2.6(7)	
		E	−0.65(1)	0.05(1)	0.54(2)	0.17(1)		−1.0	0.2	0.2		
		E	−0.66(1)	0.06(1)	0.63(0)	0.24(0)		−0.43 [c]	0.02	0.02		
297	13	A	−0.5(1)	0.0(1)								
		B	−1.16(60)	0.84(60)	0.90(0) [g]	0.70(50)		−1.78	0.96	1.49		
		C	−0.47(3)	0.13(2)	0.64(3)	0.26(3)		−2.70	0.13	0.13		
		E	−0.52(1)	0.05(2)	0.48(4)	0.13(3)		−1.4	0.3	0.2		
		E	−0.53(1)	0.05(1)	0.65(0)	0.27(0)		−0.25 [c]	0.01	0.01		

Table 3 — continued

E_γ	$2J_i$	Ref.	A_2/A_0	A_4/A_0	α_2	α_4	α_K	δ	$+\Delta\delta$	$-\Delta\delta$	δ_{DCO}	$\delta_{adopted}$
527	15	C	−0.76(5)	0.20(2)	0.79(3)	0.46(5)		−1.85	0.15	0.15		
											−0.23(7), −5.6(16)	
370	17	C	−0.65(8)	0.06(2)	0.56(5)	0.19(4)		−1.24	0.30	0.30		
		D	−0.71(11)	0.10(4)	0.65(9)	0.27(10)		−1.44	0.19	0.19		
665	19	C	−0.71(10)	0.08(3)	0.62(8)	0.24(8)		−1.26	0.32	0.32		
$\pi = +, \Delta I = 2$												
378	9	A	0.15(5)	−0.10(6)								
		C	0.28(7)	−0.07(4)	0.61(4)	0.22(3)		−0.01	0.09	0.09		
											−0.11(14)	0.0(1)
583	11	C	0.28(8)	−0.05(4)	0.61(3)	0.22(3)		0.00	0.10	0.10		0.0(1)
689	13	C	0.33(4)	−0.04(2)	0.65(2)	0.27(2)		−0.04	0.02	0.02		
		D	0.25(11)	−0.05(5)	0.59(7)	0.21(6)		−0.02	0.14	0.14		
											−0.09(11)	
		E	0.24(1)	−0.04(2)	0.57(6)	0.19(5)		−0.01	0.03	0.02		0.0(1)
824	15	C	0.42(30)	−0.05(23)	0.82(3)	0.51(6)		0.07	0.30	0.30		0.0(3)
897	17	C	0.28(30)	−0.02(11)	0.56(8)	0.19(6)		−0.02	0.11	0.11		
											−0.21(7)	0.0(2)
1035	19	C	0.10(22)	−0.09(8)	0.59(6)	0.22(6)		−0.18	0.30	0.30		0.0(4)
$\pi = -, \Delta I = 1$												
179	3	A	−0.15(1)	−0.01(1) [d]								
							0.028(3) [a,d]	0 [b]				
							0.024(6) [e,d]	0 [f]				
							0.022(3) [e,d,h]	0 [f]				
											0.00(11)	0.0(1)
179	5	A	−0.21(1)	−0.01(1) [d]								
							0.043(14) [b]	±0.6 [b]	0.3	0.3		
							0.044(18) [f]	±0.6 [f]	0.4	0.4		
							0.043(13) [f]	±0.6 [f]	0.3	0.3		±0.6(2)
607	5_2										−1.4(8)	−1.4(8)

Table 3 — continued

E_γ	$2J_i$	Ref.	A_2/A_0	A_4/A_0	α_2	α_4	α_K	δ	$+\Delta\delta$	$-\Delta\delta$	δ_{DCO}	$\delta_{adopted}$
253	7	A	−0.37(2)	−0.04(3)								
		B	−0.69(13)	0.25(13)	0.81(14)	0.50(26)		−1.18	0.11	0.23		
		C	−0.44(5)	0.03(1)	0.38(4)	0.07(2)		−1.06	0.15	0.15		
											−0.23(10), −2.5(7)	
		E	−0.52(1)	0.04(1)	0.46(3)	0.11(2)		−1.1	0.3	0.2		
		E	−0.53(1)	0.04(1)	0.60(0)	0.21(0)		−0.27[c]	0.01	0.01		
293	9	A	−0.5(1)	0.0(1)								
		C	−0.43(3)	0.03(1)	0.39(2)	0.08(1)		−1.31	0.19	0.19		
											−0.26(9), −2.9(7)	
360	11	B	−1.12(40)	0.66(35)	0.90(36)	0.80(51)		−1.67	0.52	0.83		
		C	−0.27(3)	0.03(1)	0.35(4)	0.06(2)		−2.52	0.19	0.19		
381	13	C	−0.68(7)	0.06(2)	0.58(4)	0.20(5)		−1.09	0.21	0.21		
		D	−0.61(6)	0.09(2)	0.59(6)	0.21(5)		−1.63	0.10	0.10		
											−0.04(7), −6.8(7)	
		E	−0.60(2)	0.08(3)	0.58(6)	0.21(6)		−1.6	0.3	0.2		
463	15	C	−0.28(2)	0.13(2)	0.61(4)	0.23(3)		−5.0	2.5	2.5		
453	17	C	−0.89(13)	0.17(6)	0.80(7)	0.48(13)		−1.39	0.42	0.42		
$\pi = -, \Delta I = 2$												
432	7	A	0.17(8)	−0.1(1)								
		C	0.20(13)	−0.03(5)	0.40(8)	0.08(4)		−0.03	0.05	0.05		0.0(1)
547	9	A	0.2(1)	−0.1(2)								
		C	0.20(6)	−0.03(2)	0.43(6)	0.10(3)		0.00	0.10	0.10		0.0(1)
654	11										+0.08(15)	0.0(2)
741	13	C	0.26(9)	−0.05(4)	0.61(5)	0.23(5)		−0.01	0.12	0.12		0.0(2)
844	15	C	0.29(15)	−0.06(7)	0.67(4)	0.29(5)		0.00	0.17	0.17		0.0(2)
916	17	C	0.25(35)	−0.13(21)	0.77(4)	0.44(6)		−0.07	0.34	0.34		0.0(3)
1001	19	C	0.37(51)	−0.07(34)	0.81(6)	0.51(12)		0.03	0.48	0.48		0.0(5)
660	11_2	C	0.28(19)	−0.06(10)	0.69(4)	0.32(5)		−0.01	0.21	0.21		0.0(2)

Table 3 — continued

[a] Measured in beam.
[b] Premisses: the 179_1 keV transition has a pure E1 characteristic, the relative intensities are $I_\gamma(179.0\ \text{keV}) = 240(50)$ and $I_\gamma(179.3\ \text{keV}) = 220(40)$.
[c] δ determined by constrained σ.
[d] Doublet.
[e] Measured with mass separator.
[f] Premisses: the 179_1 keV transition has a pure E1 characteristic, the relative intensities are $I_\gamma(179.0\ \text{keV}) = 90(4)$ and $I_\gamma(179.3\ \text{keV}) = 43(4)$.
[g] Error cited as published in Ref. [15].
[h] Measured at CERN; B. Fuentes and M.J.G. Borge, private communication.

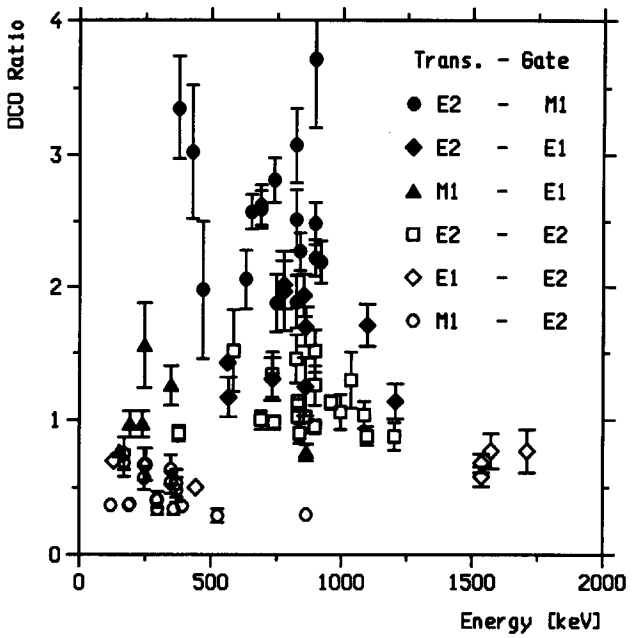

Fig. 5. DCO ratios R_{DCO} of those transitions for which multipolarity ΔI and parity-information $\Delta\pi$ is known for the transition used as gate as well as for the transition of which the line intensity is evaluated in the spectrum with $R_{DCO} = \frac{\text{Yield (gated by } \gamma_1 \text{ at } 90^\circ, \gamma_2 \text{ observed at } 25^\circ)}{\text{Yield (gated by } \gamma_1 \text{ at } 25^\circ, \gamma_2 \text{ observed at } 90^\circ)}$.

transition could be determined: 0.0(1) for 7/2→3/2→5/2, −0.5(1) for 9/2→5/2→5/2 and +0.12(5) for 11/2→7/2→5/2. Assuming, that the 179_1 keV transition is a pure E1, see also Section 2.6, we can infer from the (38°, 25°) and (25°, 38°) DCO values 0.52(8) and 0.53(8) for the 179_1–607 keV coincidence a mixing ratio for the 607 keV transition. The multipole characteristic of the 607 keV transition is a strongly mixed $\Delta I = 0$ ($\delta = -1.8(7)$) or $\Delta I = 1$ ($\delta = -1.4(8)$) transition. No agreement between experimental value and theoretical curve can be found for a 607 keV $\Delta I = 2$ transition. Because the DCO-ratio of the 577–607 keV coincidence agrees well with a stretched M1 characteristic of the 607 keV transition, we assign $\delta = -1.4(8)$ to the 607 keV transition. The mixing ratios determined by DCO are included in Table 3.

For yrast $\Delta I = 1$ transitions in the yrast bands two mixing ratio regions were determined: $\delta \approx -0.2(1)$ and $\delta \approx -3(1)$ (see also Table 3). Despite some restrictions concerning the usability of the angular correlation mixing ratios (for some strong E2 transitions the expected mixing ratio equal zero lay outside the error margins of the evaluated M3/E2 mixing ratio) these mixing ratios point, in conjunction with those from conversion electron measurements (see Section 2.5), at smaller mixing ratios compared to those determined by angular distribution in Ref. [19].

2.5. *Mixing ratios deduced by angular distributions and internal conversion*

In the course of our investigation of ^{75}Kr we measured angular distributions in coincidence with neutrons [19]. During the data analysis of the OSIRIS_10 experiment

(Ref. C in Table 3) the alignment values α_k, evaluated for an E2- and a $\Delta I = 1$ transition depopulating the same level, were checked to agree within their error bars. Thus, at least for long lived levels the mixing ratio should be determined correctly. Yet, the determined mixing ratios were incompatible with rotor model calculations [19]. The quadrupole moment ratios $R = Q_0(\Delta I = 1)/Q_0(\Delta I = 2)$ were 4–6 times larger than the ratio $R \approx 1$ expected for a prolate deformed rotor. A measurement with a mechanically new setup without neutron detectors, nevertheless, supported the large mixing ratios for ^{75}Kr [19], while small mixing ratios where extracted for ^{74}Br transitions in agreement with previous measurements. But, due to the high line density in the second experiment (Ref. D and E in Table 3) only a few angular distributions could be evaluated.

A new program [22] now calculates errors of the width of the gaussian distribution of sub-states σ and mixing ratio δ depending on the χ^2-contours, and the new fit of the angular distributions lead to minima at the same (σ, δ)-point. Compared to Ref. [19], the errors are larger and asymmetrical. The χ^2 contours for the 392 keV mixed E2/M1- and the 689 keV pure E2-transition are shown in Fig. 6. The angular distribution mixing ratio of the 191 keV transition, which shows the same banana shaped χ^2-contours as those of the 392 keV transition, is later on used for comparison with mixing ratios obtained by internal conversion coefficients. A compilation of previously reported and reanalyzed angular distribution information can be found in Table 3. The previously reported angular distribution parameters [15] yield mixing ratios $\delta \approx -1$, consistent with our angular distribution analysis, while the respective parameters A_k/A_0 published by Ref. [14] agree well with our work.

The (α_2, α_4) points determined from our angular distribution measurement (Ref. C in Table 3) were compared to the ALY-curve published in Ref. [26], which gives an upper limit for α_4-values. Although the (α_2, α_4)-error ellipses enclose the ALY-curve and with decreasing spin follow the curve in good agreement, the observed deviation in the upper direction is a hint on intensity loss due to Doppler shift, see also Ref. [26].

The very short lifetimes of ^{75}Kr levels (see Section 2.7) lead to shifts of intensity caused by DSA, which affect the angular distribution intensities analyzed via Gaussian shaped lines. The intensity loss due to Doppler shift is hard to see in case of the 689 keV transition. Nevertheless, even a relative intensity loss of 8% in case of the 689 keV line, roughly determined from DCO spectra of 90° and 25°, has certainly to be taken into account, because the overall intensity variation of an E2 angular distribution is only about 30%. Thus, angular distributions evaluated with undetected Doppler shift yield smaller alignment factors. Looking at the banana shaped χ^2 contours in Fig. 6 one easily recognizes: a larger alignment (which corresponds to a smaller σ) leads to a smaller mixing ratio δ in case of a $\Delta I = 1$ transition while the $\delta \approx 0$ value of the E2 transition remains unaffected. Taking a larger alignment into account, the mixing ratios measured via angular distribution would become reduced.

Unfortunately, it is impossible to correct quantitatively the angular distributions with regard to the DSA effect. We can only surmise the angular intensity loss due to DSA. Already the 392 and 583 keV transitions are affected by DSA. Thus, neither we have a criterion how to check the correct development of α_k in the rotational band nor can

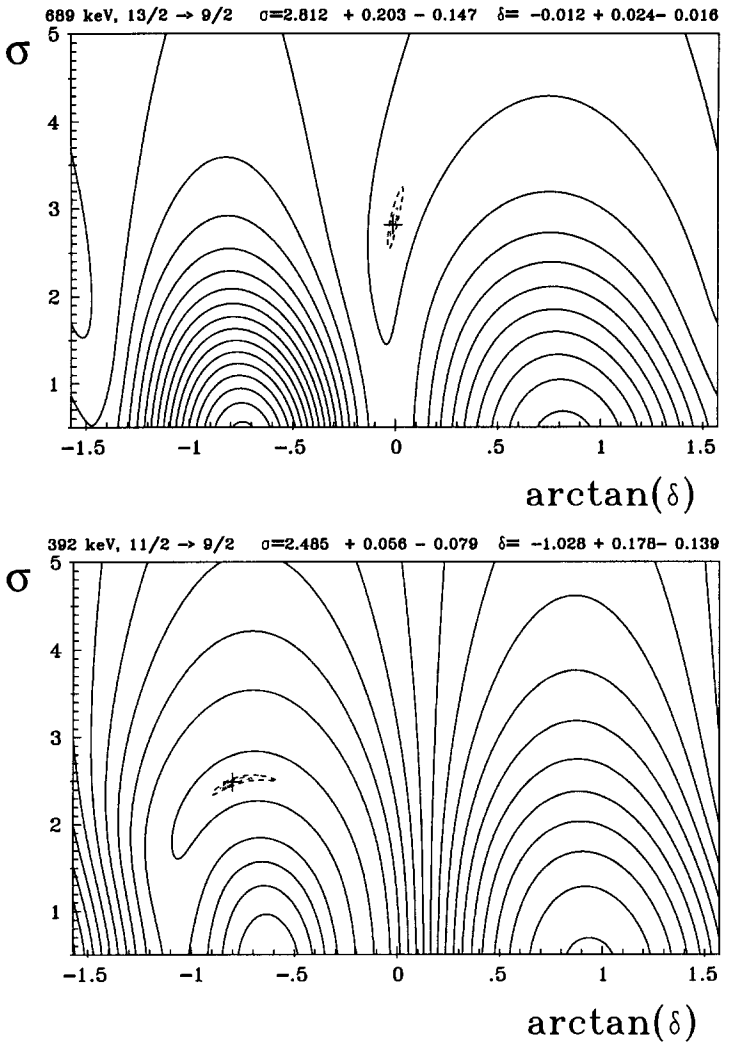

Fig. 6. χ^2 contours in dependence of the angular distribution parameters σ and δ compared for an E2 transition (689 keV, top) and a mixed E2/M1 transition (392 keV, bottom).

the correct mixing ratio be evaluated from the measured angular distribution points, except for the 191 keV and the 253 keV transition. Assuming the width of the Gaussian distribution of sub-states σ might have to be smaller than the deduced value, with a *constrained* σ corresponding an alignment of $\alpha_2 = 0.6$, E2/M1 mixing ratios of $\delta_{\text{ang}}(191\text{ keV}) = -0.29$ and $\delta_{\text{ang}}(253\text{ keV}) = -0.27$ are deducible from the measured angular distributions, see Table 3. In case of the 253 keV transition this *constrained* σ however is incompatible with the small alignment measured for the 432 keV E2 transition.

To gain mixing ratios independent of angular distributions we measured internal conversion coefficients of some low spin transitions in ^{75}Kr. Because of the small

probability for internal conversion at $Z = 36$, we could only measure the conversion coefficients of four transitions: 179 keV (doublet), 187 and 191 keV.

An excitation function was measured beforehand to optimize the reduction of interfering line intensities. To completely suppress competing ^{74}Br transitions, the reaction ^{54}Fe(^{24}Mg, 2pn)^{75}Kr was investigated at 75 MeV beam energy where the cross section for ^{74}Br is negligible. The remaining line intensities, which had to be taken into account, originated from 178 and 187 keV transitions in ^{73}Br with known conversion probabilities α_K [27]. The estimate of their intensity, based on the γ-intensities of feeding transitions, leads to an enlarged error of the ^{75}Kr electron intensities.

We used two Mini Orange systems (MO1 at 135° and MO2 at 225°) and a Ge detector at 45°. At 90° above the reaction chamber a 7 BGO γ-multiplicity filter was mounted to reduce the background. Each Mini Orange system consisted of a Si(Li) detector, cooled with liquid nitrogen, and three $SmCo_5$ magnets, each formed as an orange slice, arranged at intervals of 120° around a central Pb absorber. Electrons emitted from the target are focused through the magnets on the Si(Li) detector, and gammas are prevented from reaching the detector by the central absorber. Details of the measuring principle are to be found in Ref. [28].

A protection foil in front of the Si(Li) and pile up due to δ electron background reduced the energy resolution to 3.6 keV at 275 keV electron energy. The error of electron line intensities is based predominantly on the difficulty to fix the background, which leads to asymmetric errors. The difficulty arises from the combination of δ electrons, transmission curve, Compton continuum of the 511 keV gamma generated by pair production in the magnets, high line density and long low energy tails. The smallest possible line intensity was determined with a linear background fit of an $\exp(-x)$ background slope, thus giving the lower error margin.

The conversion probabilities α_x were evaluated with the Normalized Peak to Gamma method (NPG) [29] using the line intensities $I_{e^-}^{\exp}$ and $I_\gamma^{\exp}$ in the measured electron and gamma spectra:

$$\alpha_x = \frac{I_{e^-}^{\exp}(E_\gamma - E_x)}{I_\gamma^{\exp}(E_\gamma)} \left[\frac{\varepsilon_{e^-}(E_\gamma - E_x)}{\varepsilon_\gamma(E_\gamma)}\right]^{-1}, \tag{2}$$

with x denoting the K and L shells. To calibrate the efficiency ratio $\varepsilon_{e^-}/\varepsilon_\gamma$ we used the known conversion probabilities of transitions produced in the same reaction ^{54}Fe+^{24}Mg (^{75}Br: 119, 132, 153 and 154 keV, ^{75}Se: 287 keV) together with the Coulomb excitation of ^{181}Ta (136, 165, 302 keV) and ^{197}Au levels (191, 269, 279 keV). These transitions lead to electron lines in the right energy range 50–300 keV; the electrons are produced at the beam spot, and for ^{181}Ta and ^{197}Au the conversion probability is high due to high Z. Dead time and angular distribution effects were considered. Further, the differences between compound nucleus reaction and Coulomb excitation experiment were taken into account: alignment factors with regard to angular distribution coefficients [30] and binding energies with regard to $\varepsilon_{e^-}/\varepsilon_\gamma$.

Depending on the binding energy E_x, two γ-transitions of the same γ-energy but in nuclei of different Z lead to very different electron energies. To allow for this effect

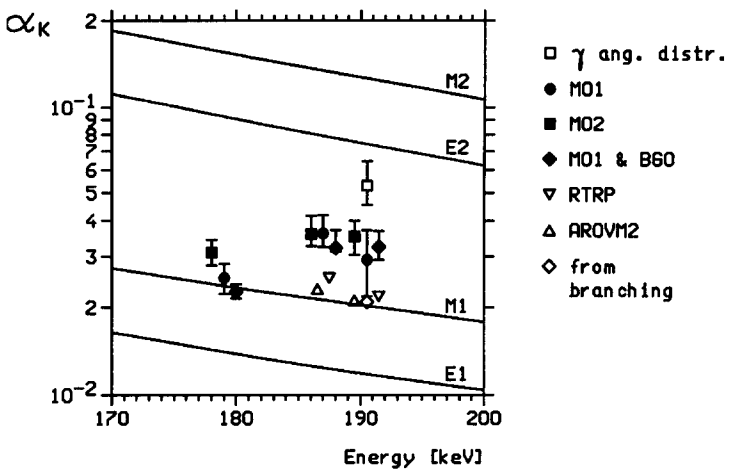

Fig. 7. Internal conversion probabilities α_K, measured with two Mini Orange systems MO1 and MO2, compared to theoretical values determined by rotor model estimate (via branching) and calculations (RTRP and AROVM2, see Section 3.2). The straight lines indicate α_K-values for unmixed transitions. For a better comparison the internal conversion probabilities of the 179 keV doublet as well as of the 187 and 191 keV transitions are moved apart. The MO1-symbol marks the correct γ-energy.

$\varepsilon_{e^-}/\varepsilon_\gamma$ has been transformed as follows:

$$\frac{\varepsilon_{e^-}(E^{\mathrm{S}}_{e^-})}{\varepsilon_\gamma(E^{\mathrm{S}}_{e^-}+14.3)} = \left[\frac{I^{\mathrm{S}}_{e^-}(E_{e^-})}{I^{\mathrm{S}}_\gamma(E_{e^-}+14.3)}\frac{1}{\alpha^{\mathrm{S}}_x}\right]\frac{\varepsilon_\gamma(E^{\mathrm{S}}_\gamma)}{\varepsilon_\gamma(E^{\mathrm{S}}_\gamma - E_x + 14.3)}, \tag{3}$$

where S denotes the calibration standard with known conversion probability α_x. Thus, the efficiency ratio $\varepsilon_{e^-}/\varepsilon_\gamma$ is adjusted to ^{75}Kr (binding energy E_{K} = 14.3 keV). All corrections considered, we determined the internal conversion coefficients for K electrons of ^{75}Kr shown in Fig. 7, the mean values are included in Table 3.

If a coincidence with a second γ was required, measured by the 7 BGO γ-multiplicity filter, the spectrum was cleaner and the error reduced, although high line density and low energy tails combined with the needed estimate of ^{73}Br transition intensities limited the improvement.

From the experimental internal conversion coefficients $\alpha_{\mathrm{K}}^{\mathrm{exp}}$ the absolute value of the mixing ratio δ was determined with

$$\delta^2_\gamma = \frac{\alpha_K(\mathrm{M1}) - \alpha_K^{\mathrm{exp}}}{\alpha_K^{\mathrm{exp}} - \alpha_K(\mathrm{E2})}. \tag{4}$$

This sign-less mixing ratio δ is also included in Table 3.

Further, we have made an independent measurement in order to elucidate the nature of the two 179 keV transitions. The investigation of the β-decay of ^{75}Rb into ^{75}Kr was carried out at the GSI on-line mass separator. The ^{75}Rb atoms were produced by bombarding a 1.6 mg/cm^2 thick ^{58}Ni target with a 84 MeV ^{20}Ne beam. The A = 75 mass activity was separated, and moreover since a mass transport system was used to move the active source from the collection to the measuring point, only the first sixty seconds after transportation were considered for the present analysis, thus avoiding the

179 keV activity in the daughter nucleus. We measured the low ^{75}Rb decay activity with a γ–e$^-$ arrangement using a Mini Orange spectrometer and a Ge detector, and a γ–X arrangement using a 40% Ge-detector and a small 2 cm thick Ge detector with 0.6 keV resolution at 122 keV. This experiment was part of a chain of investigations of mass 74,75 β-decays [31], which will be published elsewhere.

From this β-decay Mini Orange measurement an $\alpha_K = 0.024(6)$ was obtained for the 179 keV doublet in excellent agreement with the in-beam data. From the X-ray detector analysis a double fit of the complex gamma peak could be done leading to the following result: $I_\gamma(178.95(6)\ \text{keV}) = 90(4)$ and $I_\gamma(179.26(6)\ \text{keV}) = 43(4)$ in arbitrary units. The given errors include errors due to fit, calibration and shift.

From these results and the E1 character of the 178.95 keV transition (see Section 2.6) an $\alpha_K(179.26) = 0.044(18)$ and a $|\delta| = 0.6(4)$ value could be extracted. This result from a contamination free experiment provides a completely independent measurement of the E2/M1 mixing ratio δ, which again points to a larger E2 admixture. These results are also included in Table 3.

Comparison with mixing ratios determined by theoretical model calculations ([19] and Section 3.2) and by angular distribution measurement shows us that neither determination agrees with the internal conversion. Already the $\alpha_K(191\ \text{keV})$-value, determined from a mixing ratio evaluated via Alaga rules by the branching ratio, deviates from the measured α_K (see Fig. 7). The banana shaped χ^2 contours allow smaller E2/M1 mixing ratios δ when the alignment dependent parameter σ is fixed to smaller values. For pure E2 transitions this parameter has smaller margins. Thus, the angular distribution coefficient δ of a mixed $\Delta I = 1$ transition can be pushed to agree with the mixing ratio determined from internal conversion probabilities. Because of the problems discussed in this chapter we do not propose adopted values for most of the E2/M1 mixing ratios.

The mixing ratios determined by internal conversion yield the adopted mixing ratios $\delta_{\text{conv}}(187\ \text{keV}) = -0.55(6)$, $\delta_{\text{conv}}(191\ \text{keV}) = -0.56(7)$, and $\delta_{\text{conv}}(179_2\ \text{keV}) = \pm 0.6(2)$. These values are considered as the most trustworthy, because three independent internal conversion measurements yield the same mixing ratio for the 179_2 keV transition.

Therefore, to include all known experimental information (internal conversion, DCO and angular distribution for the utmost maximum value) we will use for comparisons with theoretical calculations an experimental mixing ratio $\delta = -0.6(4)$ for transitions depopulating the higher excited levels. Due to this large experimental error of 75% the errors of the affected $B(\text{E2}, \Delta I = 1)$-values ($\propto \delta^2/(1+\delta^2)$) have an error of 98% while the $B(\text{M1})$-values ($\propto 1/(1+\delta^2)$) have only an error of 36%. Nevertheless, with $|\delta(191\ \text{keV})|_{\text{conv}} = 0.56(7)$ we infer for the 378 keV level a $Q_0(\Delta I = 1)/Q_0(\Delta I = 2)$-ratio of $R = 2.54(26)$ which differs significantly from a theoretically expected $R \approx 1$, see also Ref. [19].

2.6. The level scheme

The proposed level scheme, Fig. 8, was established based on $\gamma\gamma$-coincidences, intensities, angular distributions and correlations, internal conversion coefficients and excitation functions.

A ground-state spin and parity of $I^{\pi} = 5/2^{+}$ was assigned to ^{75}Kr in all previous investigations. Arguments from β^{+}-decay data fix the the positive parity and with large probability spin 5/2 ([14,19]). However, a spin of 3/2 could not be excluded definitely until recently hyperfine structure investigations by Keim et al. using laser spectroscopy pinned down the ground-state spin to 5/2 [32].

The band-head spin of the negative parity band could not be determined until now because of a 179 keV doublet, although all investigators assumed consistently 3/2 based on model calculations. Both yrast bands have nearly the same large deformation deduced from measured lifetimes (see Section 2.7). The sign of the measured mixing ratios points to prolate deformation for both yrast bands. Since both yrast bands have almost the same large prolate deformation, there is no reason why they should not decay into one another if they were of the same positive parity. But in the present investigation beside the known 358 keV transition only two new, very weak inter-band transitions (171 and 234 keV) were found. Further, ^{75}Rb decays predominantly into levels belonging to the rotational band on the 179 keV state. Although a negative parity of the ^{75}Rb ground state is not certain, again there is no reason why the ^{75}Rb ground state should not decay in similar quantities into states of both yrast bands if there are no differences in deformation, spin or parity. In conclusion, the opposite parity is most probable for the second band-head.

The conversion electron measurement yielded a mean $\alpha_K = 0.028(3)$ for the 179 keV doublet, thus resembling a pure M1 transition. The similar relative intensities of the two 179 keV transitions imply a $\Delta I = 0, 1$ multipolarity for both. Therefore the band-head spin must be 3/2, 5/2 or 7/2. The band-head spin 7/2 can be excluded because no such Nilsson single particle state with negative parity can be found for $N = 39$. The angular correlation between the 432 keV E2 transition and the 179_1 keV transition yields a pure $\Delta I = 1$ transition ($\delta = 0.0(1)$) for the spin hypothesis $7/2 \rightarrow 3/2 \rightarrow 5/2$. Thus, the 179_1 keV transition could be a pure E1, which would demand a mixed 179_2 keV transition or both 179 keV transitions have to be a pure M1 to reproduce the measured α_K. In case of the $9/2 \rightarrow 5/2 \rightarrow 5/2$ hypothesis a large quadrupole admixture ($\delta = -0.5(1)$) for the 179_1 keV transition is determined. This large admixture would have to be compensated by a pure E1 characteristic of the 179_2 keV transition to result for the 179 keV doublet in the seemingly pure M1 characteristic determined by the conversion electron measurement.

The spin of the 358 keV level can be limited to $(1/2, 5/2, 9/2)$ because of the $\Delta I = 0, 2$ multipolarity determined by DCO for the 358 keV transition. The spin of the 611 keV level can be determined by the 234 keV inter-band transition to the $9/2^{+}$ level. The branching ratio of 2% and the 611 keV level lifetime lead to an E1 transition. Thus, the parity of the 611 keV level is fixed as negative, and the spin is limited to

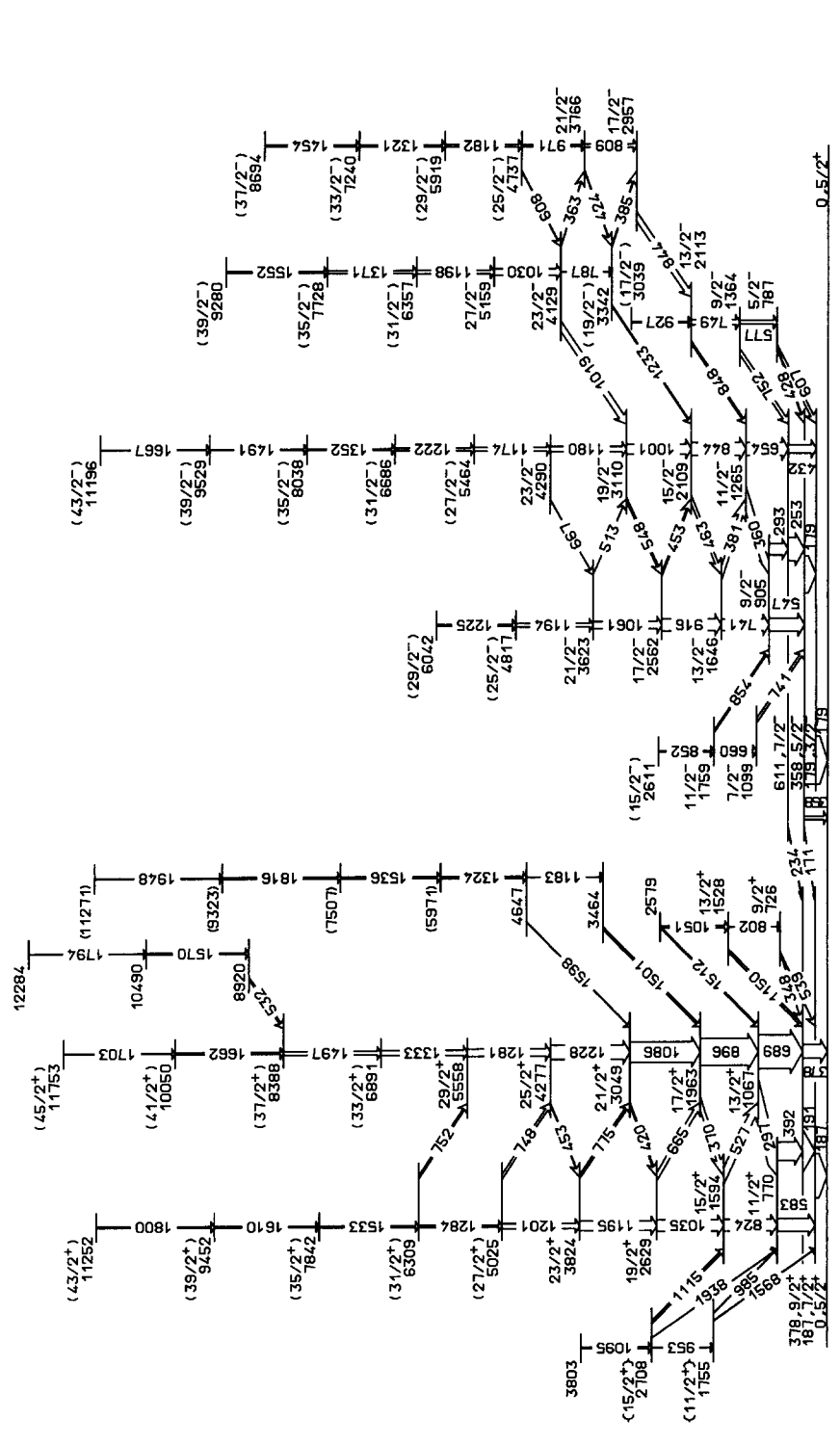

Fig. 8. Proposed level scheme for ^{75}Kr: levels and intensities were obtained from the reactions ^{54}Fe(^{24}Mg,2pn) and ^{58}Ni(^{20}Ne,2pn)^{75}Kr. Spins and parities were deduced from conversion electron (^{54}Fe(^{24}Mg,2pn)^{75}Kr) and angular distribution (^{50}Cr(^{28}Si,2pn)^{75}Kr) as well as angular correlation (^{58}Ni(^{20}Ne,2pn)^{75}Kr) measurements.

(7/2, 9/2, 11/2). The E2/M1 characteristic of the 253 keV and the E2 characteristic of the 432 keV transition then fix the spin of the 611 keV level. The $11/2^-$ is excluded because a band-head spin of $7/2^-$ is not possible. A $9/2^-$ would lead to a large M2 admixture for the 179_1 keV transition, because of the mixing ratio determined by angular correlation analysis. This large M2 admixture would have to be compensated by a pure E1 characteristic of the 179_2 keV transition to reproduce the α_K measured in the conversion electron measurement. But a positive parity of the 358 keV level is excluded by the E2/M1 characteristic of the 253 keV transition. Thus, by exclusion of $11/2^-$ and $9/2^-$, spin and parity of 611 keV level is fixed to $7/2^-$.

Having thus fixed $7/2^-$ of the 611 keV level, spin and parity of the 358 keV level is fixed to $5/2^-$ by the 253 keV transition. And the E2 characteristic of the 432 keV transition fixes the $3/2^-$ of the 179 keV level. In summary, there are many interwoven experimental facts which fix spin and parity of the first excited state in ^{75}Kr to $3/2^-$.

The spins of the low energy levels feeding into the yrast bands were determined by DCO ratios (see Table 2), angular distributions (see also Ref. [19]) and excitation functions [19,25]. All spins in parentheses were proposed, as usual for deformed nuclei, based on the assumption of increasing spin and E2 transitions. The braces denote a spin determination based on not fully definite DCO ratios.

The transition 848 keV between the 2957 keV and the 2109 keV level was seen neither gated by the 463 keV nor gated by the 381 keV transition and thus has been rejected.

2.7. Lifetimes

The nucleus ^{75}Kr has been interpreted as to have a large prolate deformation of $\beta_2 \approx 0.4$ (Ref. [13–19]). On the other hand, the conversion electron measurement yielded mixing ratios of $\delta \approx -0.6$, unexplainable by rotor models (see Ref. [19] and Section 3.3). Therefore, we searched for other deviations from expected features generated by prolate deformation as for instance B(E2) and B(M1) values. To reduce the high line density of heavy ion reactions we measured the lifetimes in coincidence. Even better, if the chosen gate transition precedes the investigated, only the experimentally observed feeding has to be considered in the lifetime analysis.

The lifetimes were measured as described in Section 2.2. The measurement was performed with a plunger system described in Ref. [33] (self-supporting ^{54}Fe target and ^{181}Ta recoil stopper). The recoil distance Doppler shift was measured for six target-stopper distances (96, 47, 39, 30, 19, 12 μm). Due to the recoil velocity, v/c = 2.25(3)%, flight and stop peak were separate down to 250 keV.

The distances were measured in-beam by the capacity between target and stopper foil. The capacity as a function of distance was calibrated off-beam by measuring the distances in the 0–200 μm range (0.1 μm error) with a magnetic transducer. For target currents of more than 80 nA the capacity values wildly leaped to higher values. This was explained after the experiment by a bump on the target foil caused by thermal expansion at the beam spot [34]. During the lifetime measurement we held capacity

Table 4
Lifetimes, reduced transition probabilities and quadrupole moments for ^{73,75}Br, ^{72}Se and ^{76}Kr.
Because of the reduced possibilities for systematic errors, due to the gating from above, the τ_{DDCM}-values are taken as adopted values. Legend: E_x = excitation energy (keV), E_γ = transition energy (keV), τ = lifetime (ps), τ_{single}: deduced from singles data, τ_{DSA}: deduced from coincidence data, τ_{DDCM}: deduced by DDCM from coincidence data, this work

	Spin	E_x (keV)	E_γ (keV)	τ_{single} (ps)	τ_{DSA} (ps)	τ_{DDCM} (ps)	B(E2) (e^2b^2)	$\|Q_t\|$ (b)
^{73}Br, $\pi = +$ ($K = 3/2$)	13/2	1057	583	4.8(4)[a]		5.7(11)	0.21(4)	2.8(5)
	17/2	1862	804	2.2(5)[a]	1.3(3)[a]	1.0(5)	0.2(1)	2.8(14)
^{75}Br, $\pi = -$ ($K = 3/2$)	7/2	518	518	14.7(10)[b]		10.2(7)	0.17(1)	3.4(3)
	11/2	1150	632	3.9(7)[b]		3.3(1)	0.24(1)	3.1(2)
	17/2	1897	747	1.8(9)[b]		1.1(1)	0.32(3)	3.3(3)
	19/2	2756	859	1.2(3)[b]	0.9(2)[b]	0.8(2)	0.22(6)	2.6(7)
^{72}Se, $\pi = +$ ($K = 0$)	2	863	863	3.4(3)[c]		2.6(1)	0.065(3)	1.81(7)
				4.0(5)[c]				
				4.8(6)[d]				
				5.2(5)[e]				
				5.7(12)[f]				
				3.1(6)[g]				
	4	1637	775	2.4(3)[c]	4.5(13)[f]	2.1(1)	0.14(1)	2.2(1)
				2.7(3)[c]				
				3.8(5)[d]				
				2.7(3)[e]				
				1.2(3)[g]				
	6	2467	830	2.6(5)[c]	1.6(3)[d]	1.4(1)	0.15(1)	2.2(2)
				2.2(3)[e]	2.6(7)[f]			
				$\leqslant$0.7[g]				
^{76}Kr, $\pi = +$ ($K = 0$)	2	424	424	36(1)[h]		31(3)	0.19(2)	3.1(3)
				34(2)[h]				
				35(3)[j]				
				53(7)[l]				
	4	1035	611	4.9(4)[h]	5(2)[k]	3.0(3)	0.32(3)	3.3(3)
				4.2(10)[i]				
				4.8(9)[j]				
				8.2(23)[l]				
	6	1859	824	1.5(2)[h]	1.18(13)[m]	0.8(3)	0.3(1)	2.9(11)
				0.8(2)[i]	1.25(12)[k]			

[a] Ref. [37], [b] Ref. [38], [c] Ref. [39], [d] Ref. [40], [e] Ref. [41], [f] Ref. [42], [g] Ref. [43], [h] Ref. [44], [i] Ref. [45], [j] Ref. [46], [k] Ref. [8], [l] Ref. [47], [m] Ref. [48].

and event rate stable. Thus, an unreproducible distance reduction due to a target bump was avoided.

For the determination of the lifetimes we used the Differential Decay Curve Method (DDCM) developed by Dewald et al. [35]. In the simplest case a direct feeder is used as a gating transition. Gating on the flight peak of a feeding transition for different target-stopper distances the flight and stop peak intensities Int^{Stop} and Int^{Flight} of the investigated transition are determined in those spectra, where the feeding transition occured in flight. For this simple case the lifetime is evaluated with the equation

Table 5
Lifetimes, reduced transition probabilities and quadrupole moments for ^{75}Kr.
Because of the reduced possibilities for systematic errors, due to the gating from above, the τ_{DDCM}-values are taken as adopted values if determined. The error of the $B(E2)$-value takes into account the error of the branching ratio, therefore also the lower limits of $B(E2)$ and $|Q_t|$ are given with errors. Legend: E_x = excitation energy (keV), E_γ = transition energy (keV), τ = lifetime (ps), τ_{single}: deduced from singles data [18], τ_{DDCM}: deduced by DDCM from coincidence data, this work

	Spin		E_x	E_γ	τ_{single}	τ_{DDCM}	$B(E2)$	$\|Q_t\|$
	initial	final	(keV)	(keV)	(ps)	(ps)	(e^2b^2)	(b)
^{75}Kr, $\pi = +$ ($K = 5/2$)	7/2	5/2	187	187	52(5)[a]			
	9/2	5/2	378	378	31(3)[a]	20.0(16)	0.14(1)	3.8(4)
	11/2	7/2	770	583	4.6(12)[a]	2.50(16)	0.20(1)	3.4(2)
	13/2	9/2	1067	689	<3.6[a]	1.9(1)	0.20(1)	3.1(2)
	15/2	11/2	1594	824		<0.5	>0.25(1)	>3.1(2)
	17/2	13/2	1963	896		<0.9	>0.13(1)	>2.2(1)
^{75}Kr, $\pi = -$ ($K = 3/2$)	3/2	5/2$^+$	179	179	3000(500)[a]			
	5/2	3/2	358	179	62(15)[a]			
	7/2	3/2	611	432	15(2)[a]	8.42(35)	0.17(1)	3.4(2)
	9/2	5/2	905	547	3.6(10)[a]	2.9(6)	0.27(6)	3.6(8)
	11/2	7/2	1265	654	<4[a]	1.1(3)	0.38(11)	3.9(11)
	13/2	9/2	1646	741		1.0(3)	0.25(8)	3.0(9)
	15/2	11/2	2109	844		<0.6	>0.26(1)	>2.9(2)

[a] Ref. [18].

$$\tau(t_j) = \frac{\mathrm{Int}^{\mathrm{Stop}}(t_j)}{\mathrm{Int}^{\mathrm{Flight}}(t_{j-1}) - \mathrm{Int}^{\mathrm{Flight}}(t_{j+1})} \times (t_{j-1} - t_{j+1}) , \tag{5}$$

where t_j denominates the flight time for the plunger distance j. Further information about DDCM can be acquired in Refs. [35,36].

To test systematic errors, lifetimes for nuclei of various evaporation channels were determined. Table 4 lists lifetimes τ_{DDCM} for ^{73,75}Br, ^{72}Se and ^{76}Kr and compares them to previously published data. Lifetimes measured in coincidence agree well with our values. Deviating lifetimes measured via single spectra can be explained by wrong assumptions about feeding times, feeding patterns and/or unknown and thus unconsidered feeders (Ref. [8,37–48]). For instance, in ^{72}Se the transitions 1303, 1338, 1450, 1537, 1571 and 1713 keV all depopulate longer lived states (showing little Doppler shift) and feed into the yrast band. Further, a transition with $E_\gamma = 2098$ keV populating the 7037 keV yrast state was found also showing little Doppler broadening. Such longer lived states were also found in ^{73}Br. The influence of such an unconsidered feeding transition has been shown by Dewald et al. [35].

The overall comparison of ^{73,75}Br, ^{72}Se and ^{76}Kr lifetimes reveals: when measured in coincidence the deduced lifetimes are obviously shorter. The same applies to lifetimes of ^{75}Kr states. Fig. 9 shows the 689 keV transition intensities gated by the flight peak of the direct feeders 527 and 896 keV for the distances 12, 19, 30, 39, 47 and 96 μm and the derived lifetimes. Table 5 lists lifetimes, measured in coincidence and evaluated by DDCM, and compares them to lifetimes published by Cardona et al. [18]. The

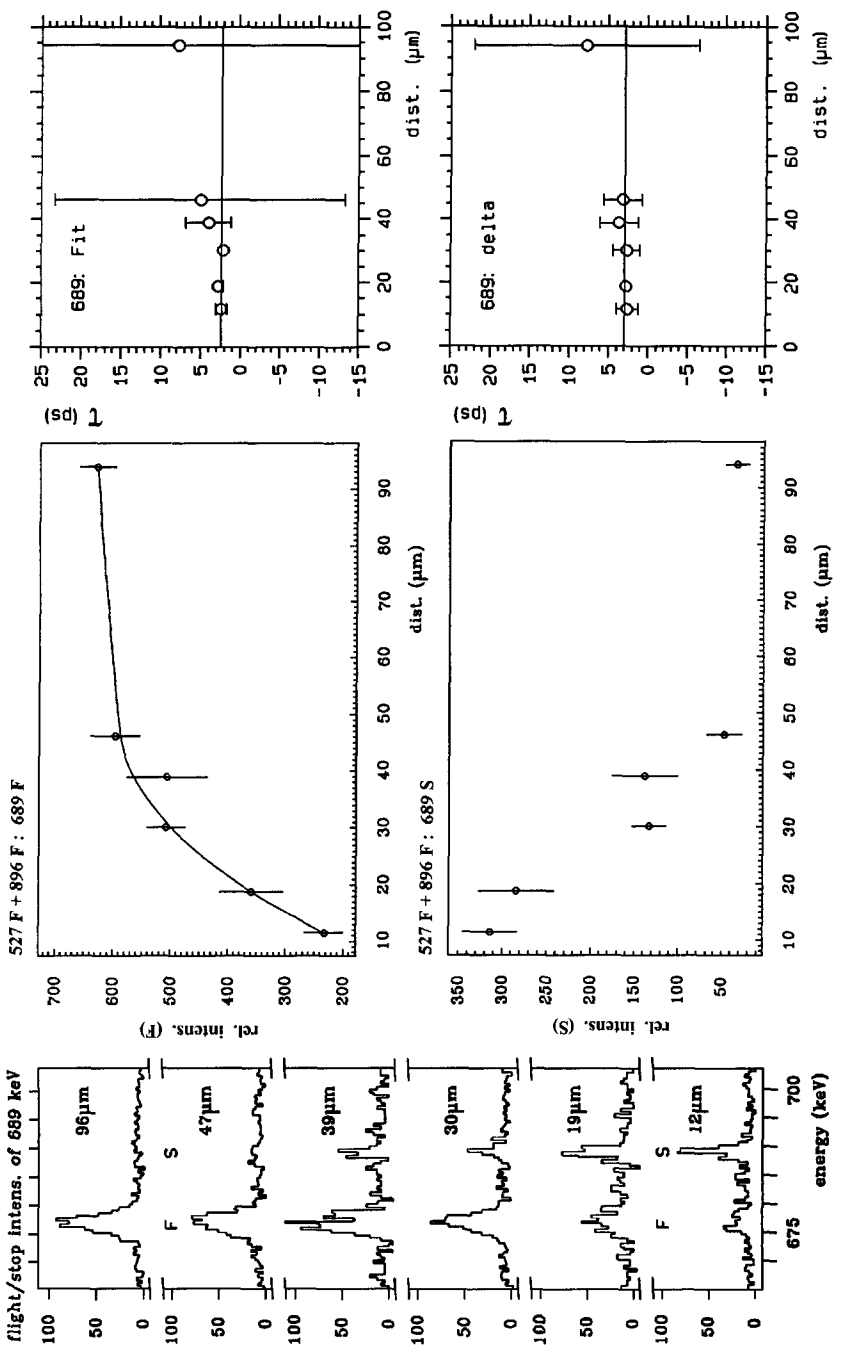

Fig. 9. Evaluation of a ^{75}Kr level lifetime measured in coincidence. Gating on the flight peak of the 527 and 896 keV transition these direct feeders of the 1067 keV level yield a flight and a stop peak of the 689 keV transition per distance. (left) The corresponding part of the spectra (flight indicated by F and stop by S). (middle) The determined intensities are presented in dependence on the flight distance. (right) The lifetime τ is evaluated by applying Eq. (5) either on the values given by the curve fitted to the flight peak intensities (top, indicated by fit) or on the measured intensities (bottom, indicated by delta).

deviations can be explained by the previously unknown and therefore not considered feeding from the new sidebands at low excitation energy (see also Ref. [35]).

The very short lifetimes in ^{75}Kr hint at a large prolate deformation. Comparing the quadrupole moments Q_t listed in the Tables 4 and 5, measured via the $B(E2)$ value determined from τ_{DDCM}, evidently ^{75}Kr is more deformed than its neighboring nuclei, and thus it is one of the most deformed neutron-deficient nuclei in the mass region $A \approx 70-80$.

3. Interpretation of ^{75}Kr

The strong coupling band structure and large quadrupole moments point obviously at a large deformation. Therefore, we used the Cranked Shell Model (CSM) to gain insight concerning deformation, aligning pairs and critical frequencies. And we applied two different rotor models to reproduce excitation levels, $B(E2)$ and $B(M1)$ transition probabilities.

To compare the experimental deformation β_2 derived from measured transition quadrupole moments with those used in model calculations as cranking model or rotor model, one has to consider the charge distribution used. Usually the experimental β_2 is calculated for axially symmetric deformation with $\beta_2^{\rho,\text{sharp}}(\gamma = 0) = 91.7Q_0/ZA^{2/3}$ for a sharp nuclear surface. This would give super-deformations $\beta_2 \approx 0.5$ for the rotational bands in ^{75}Kr ($\beta_2 = 0.47(2)$ for positive parity and $\beta_2 = 0.49(3)$ for negative parity. Thus, ^{75}Kr is one of the most deformed nuclei found in the nuclear chart. But, the diffuse nuclear surface is better described by a Woods–Saxon-potential leading to [49] $\beta_2^{\rho,\text{diff}} = \beta_2^{\rho,\text{sharp}}[1 - (4/3)\pi^2(a/R_0)^2]$ which reduces the β_2 by a factor of 0.87 to 0.88 in the mass region $A \approx 70-80$. Thus, we get $\beta_2^{\rho,\text{diff}} = 0.41(2)$ for positive and $\beta_2^{\rho,\text{diff}} = 0.43(3)$ for negative parity. The deformation of the positive parity yrast states, obtained by $B(E2)$ values, agrees well with the deformation values published in Ref. [32] for the ground state of ^{75}Kr: assuming a strong coupling scheme the intrinsic quadrupole moment was determined as $Q_0 = 3.1(4)$ b corresponding to $\beta_2 = 0.43(5)$.

3.1. Cranking model

The kinematic and dynamic moments of inertia, Fig. 10, present a straight line up to $\hbar\omega = 0.6$ MeV for ^{75}Kr. Thus, up to spin 21/2 rotor model calculations should reproduce all experimental features. In order to understand the structure of ^{75}Kr, cranking calculations based on the deformed Woods Saxon potential have been performed. Details of these calculations are given in Ref. [1]. The used model calculations GAMLAT for the Total Routhian Surfaces (TRS) were performed with pairing and were minimized with respect to the hexadecupole deformation β_4 at each (β_4, γ) mesh point. The TRS, Fig. 11, show a stable absolute minimum at prolate deformation ($\gamma = 0°$) and a second minimum at oblate deformation ($\gamma = -60°$). The oblate minimum disappears

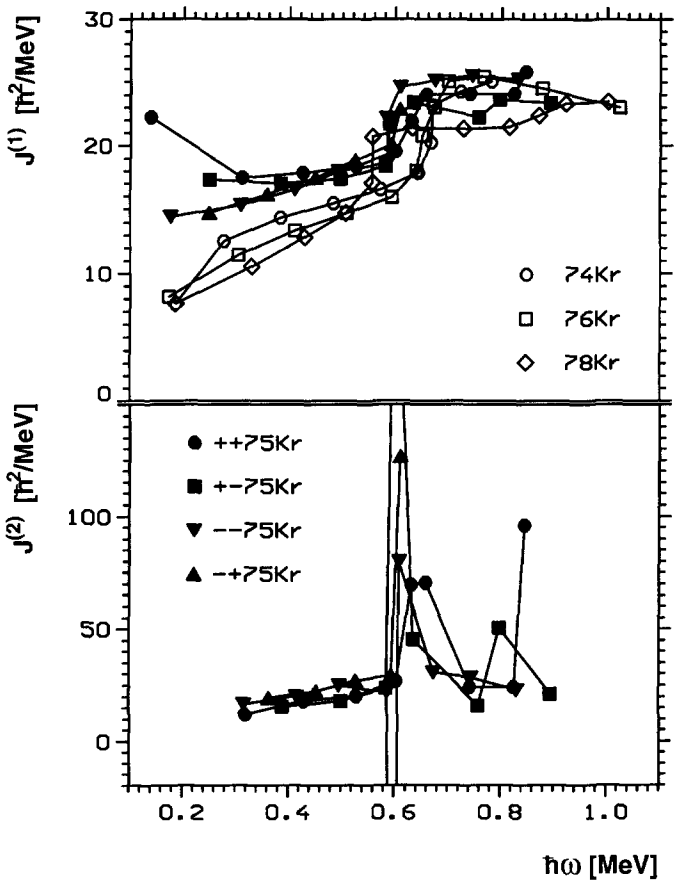

Fig. 10. Moments of inertia. (top) Kinematic moments of inertia $J^{(1)}$ in the four main bands of ^{75}Kr (different in parity π and signature α) compared to the even isotopes ^{74,76,78}Kr. (bottom) Dynamical moments of inertia $J^{(2)}$ in the four main bands of ^{75}Kr. Legend: (parity π, signature α): (+,+), (+,−), (−,+), (−,−).

at 0.6 MeV rotational energy, the same energy where the loss in pairing correlations occurs.

Compared to the CSM-values of $\beta_2 = 0.37$ (positive parity) and $\beta_2 = 0.35$ (negative parity) the experimental values $\beta_2^{\rho,\mathrm{diff}} = 0.41(2)$ for positive and $\beta_2^{\rho,\mathrm{diff}} = 0.43(3)$ for negative parity are more than 10% larger. This deviation might be due to the pn-interactions not incorporated in the CSM calculations.

Calculations of the Routhians with JXGAMAVR, SWGEST and SFBAVR, Fig. 12, show that the first aligning nucleons are of positive parity, thus they must originate in the $g_{9/2}$ shell. For protons, only the calculations for the ground-state band (minimum at $\beta_2 = 0.37$, $\beta_1 = 0.0$, $\gamma = 0.0$) are shown (Fig. 12, left). For the negative-parity band (minimum at $\beta_2 = 0.35$, $\beta_1 = 0.01$, $\gamma = -2.0$) the figure is very similar and results in the same critical frequency. For neutrons, the calculations were performed likewise with the respective TRS minimum values. In the negative parity band the alignment of a $g_{9/2}$ pair occurs simultaneously for protons and neutrons at $\hbar\omega = 0.53$ MeV (Fig. 12,

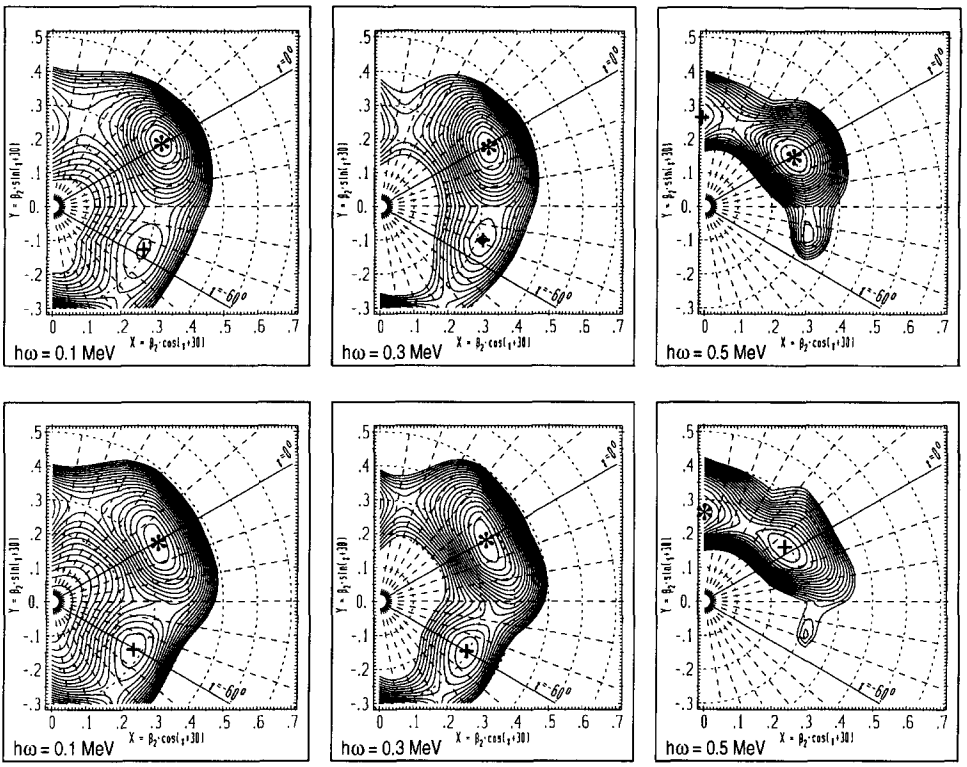

Fig. 11. Total Routhian Surfaces calculated for increasing rotational energy in the 1qp bands of ^{75}Kr: positive parity top, negative parity bottom. Legend: —— energy contours are shown in 100 keV intervals, * absolute minimum, + relative minimum.

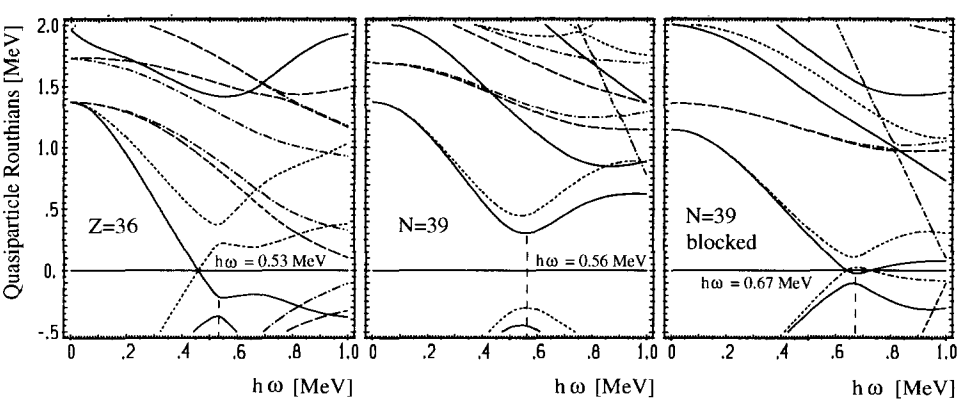

Fig. 12. Routhians: the proton Routhians are calculated for the positive parity $g_{9/2}$ band in ^{75}Kr at the $(\beta_2, \beta_4, \gamma) = (0.37, 0.0, 0°)$ point of the prolate deformed minimum in the TRS (left). At $(\beta_2, \beta_4, \gamma) = (0.35, 0.01, -2°)$, the prolate minimum calculated for negative parity, the proton Routhians are showing nearly the same slopes. The neutrons are calculated for the respective minimum without (middle, negative parity) and with (right, positive parity) blocking of pair alignment due to an unpaired neutron. Legend: (parity π, signature α): $(+,+)$ ——, $(+,-)$ – – – –, $(-,+)$ — — — —, $(-,-)$ —·—·—·—.

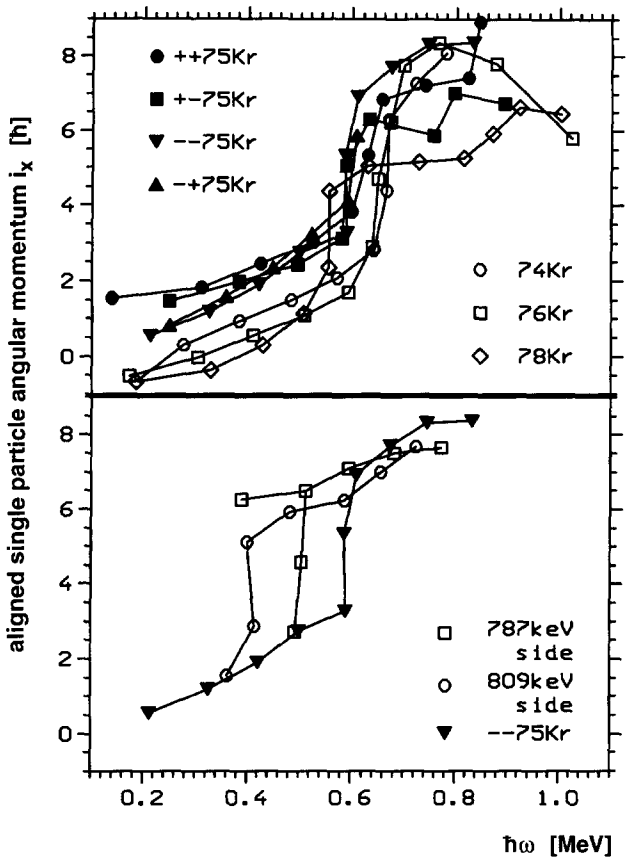

Fig. 13. Aligned single particle momentum i_x (reference $J_0 = 11\hbar^2/\text{MeV}$ and $J_1 = 6\hbar^4/\text{MeV}^3$). (top) Comparison between yrast bands. (bottom) Comparison between negative parity side bands and negative parity yrast band, the 3qp band signature partners are labeled by the respective first E2-transition. ^{75}Kr: $\pi+$: $K = 5/2$, $\pi-$: $K = 3/2$, even even nuclei: $K = 0$. Legend: (parity π, signature α): $(+,+)$, $(+,-)$, $(-,+)$, $(-,-)$.

middle). In the positive parity band, on the other hand, the $g_{9/2}$ neutron blocks the [422]5/2 single particle state shifting the $g_{9/2}$ neutron alignment up to $\hbar\omega = 0.67$ MeV (Fig. 12, left).

These theoretical findings agree qualitatively with the behavior of the experimental alignment i_x shown in Fig. 13 (upper part). The core parameters $\mathcal{J}^0_{\text{ref}} = 11\hbar^2/\text{MeV}$ and $\mathcal{J}^1_{\text{ref}} = 6\hbar^4/\text{MeV}^3$ were taken from Ref. [50]. Therein the adapted g-reference was determined from regions of near constant deformation found in ^{75}Br, ^{77}Rb and ^{78}Kr. The parameters were adjusted until the alignment curves in these regions were approximately constant. Thus, the Coriolis alignment of the single particle spin should be accounted for. Both yrast bands show a step in the alignment enhancement at $\hbar\omega = 0.6$ MeV. The gradual enhancement below 0.6 MeV can be attributed to the Coriolis anti pairing effect. Thus, combining the alignment gain of about $2\hbar$ through the Coriolis anti pairing effect and the alignment step at $\hbar\omega \approx 0.6$ MeV up to $6\hbar$, the total alignment gain

$\Delta i_x \approx 5\hbar$ must originate from an aligning $g_{9/2}$ pair. The $g_{9/2}$ band shows a second enhancement at $\hbar\omega \approx 0.8$ MeV, which according to CSM calculations can be explained by the alignment of an $g_{9/2}$ neutron pair hindered at low excitation energy by an occupied $\Omega = 5/2$ state. Therefore, the first alignment affects a proton pair. The positive signature partner of the negative parity band is not observed above the alignment step at $\hbar\omega \approx 0.6$ MeV. The large alignment enhancement in the negative signature partner of the negative parity band, saturating at $\hbar\omega = 0.7$ MeV and $i_x = 8\hbar$, is explained according to CSM calculations by a simultaneous alignment of both a $g_{9/2}$ proton- and a $g_{9/2}$ neutron-pair in the region $\hbar\omega = 0.6$–0.7 MeV leading to a negative parity 5qp band. This interpretation accords with interpretations of neighboring nuclei (^{74}Kr [10], ^{75}Br [51], ^{76}Kr [50]).

The negative parity 1qp yrast band is populated by a strong 1019 keV transition which depopulates a $23/2^-$ (4129 keV) level. Upwards the sideband is yrast. The lowest level of the 3qp sideband is observed at 2957 keV with $17/2^-$. There are a number of negative parity 3qp band heads reported in neutron-deficient $A \approx 80$ nuclei, e.g. ^{77,79,81}Br, ^{79}Kr and ^{79,81,83}Rb. Those bands are interpreted by Tabor and Döring to originate from a $\pi(pf) \otimes \pi(g_{9/2}) \otimes \nu(g_{9/2})$ configuration [52]. One might compare the characteristics of those sidebands with the present negative parity band in ^{75}Kr. The configuration $\pi(pf) \otimes \pi(g_{9/2}) \otimes \nu(g_{9/2})$ should decay into both the yrast bands of either parity. This is definitely not the case for the sideband on the 2957 keV level. In contrast to the characteristics of a $\pi(pf) \otimes \pi(g_{9/2}) \otimes \nu(g_{9/2})$ band, the $\Delta I = 2$-transitions are stronger than the $\Delta I = 1$-transitions and a signature splitting can be observed. We conclude, that the negative parity 3qp sideband in ^{75}Kr probably has another configuration.

The negative signature partner of the negative parity 1qp sideband ends at a rotational frequency $\hbar\omega \approx 0.4$ MeV, while the positive signature partner shows at this frequency an up-bending of about $\Delta i_x = 4\hbar$. This alignment occurs at a definitely lower critical rotational frequency than for the negative parity yrast band (Fig. 13, lower part). The 1019 keV transition is represented by the open square in Fig. 13 at $\hbar\omega = 0.5$ MeV and $i_x = 4.5\hbar$, the 844_{side} keV transition by the open circle at $\hbar\omega = 0.42$ MeV and $i_x = 5\hbar$. Further, the 3 qp sideband depopulates through two quite different paths. The 3qp sideband of negative signature, labeled "787 keV side" in Fig. 13, decays as expected via a strong branch into the 1qp negative signature yrast band (1019 keV, $23/2^-_1$ (4129 keV)$\rightarrow 19/2^-_1$ (3110 keV)). Curiously enough, the 3qp sideband of positive signature, labeled "809 keV side", does not decay into the positive signature yrast (unfavoured) band but decays via the 844_{side} keV transition into the yrare 1qp sideband. Thus, we suspect a fundamental structural difference between the 1qp positive signature main band and the 1qp and 3qp sideband of positive signature, a difference larger than expected for a prolate deformed nucleus.

The theoretical Routhians, calculated for protons and neutrons without blocking at $\beta_2 = 0.31$ and $\gamma = -50°$ given by the second minimum in the TRS, show for the protons a loss in pairing correlations with a strong interaction at $\hbar\omega \approx 0.65$ MeV and a neutron pair alignment at $\hbar\omega \approx 0.48$ MeV. Thus, a calculation with oblate deformation reproduces the low energy up-bending in the negative parity sideband. The

strong interaction between the proton states might explain the hidden second up-bending.

3.2. Rotor model

The Cranking Model showed the development of intrinsic states in ^{75}Kr as a function of the rotational energy. Now the energy levels and the $B(M1)$ and $B(E2)$ transition probabilities shall be reproduced by models coupling a quasi-particle to a rotating core.

The Rigid Triaxial Rotor + Particle (RTRP) model couples a particle roaming deformed orbitals to a rigid rotor (constant moment of inertia) [53]. At first, the single particle energies are calculated for the deformation $\varepsilon \approx 0.95\beta$ and triaxiality γ. For positive parity the following shell model states, given according to their increasing single particle energies, and their Ω sub-states are considered: $1s_{1/2}$, $1d_{5/2}$, $2s_{1/2}$, $1d_{3/2}$, $1g_{9/2}$, $2d_{5/2}$, $1g_{7/2}$, $3s_{1/2}$, and $2d_{3/2}$ as for negative parity: $1p_{3/2}$, $1p_{1/2}$, $1f_{7/2}$, $2p_{3/2}$, $1f_{5/2}$, and $2p_{1/2}$. Nilsson states are mixed by small deformation or triaxiality. Up to fifteen of these mixed states can be selected to calculate energy levels and electro-magnetic characteristics. The Coriolis attenuation has been estimated as 0.5 for the high spin $g_{9/2}$ orbit by using the self-consistent attenuation factor $I_x = 1 - i_x/I_x$ [54]. For the low spin negative parity band the Coriolis attenuation can be ignored. The core is taken into account via its 2_1^+ energy, which is represented for ^{74,76}Kr by an estimated undisturbed mean level energy of $E(2_1^+) = 224$ keV [8]. Data from β^+-decay of ^{75}Rb concerning low spin levels in ^{75}Kr constricted possible triaxiality values to less than 15° for negative parity and to less than 20° for positive parity (see also Refs. [15,19]). To include effects due to a possible triaxiality the rotor model calculations (Table 6) were performed with a triaxiality value $\gamma = 15°$.

The RTRP model calculations (Table 6) are compared to calculations with the Asymmetric Rotor with Variable Moment of inertia, where the coupled particle can occupy only two shell model states (AROVM2) [55–58]. The fit of model parameters has been described in Ref. [19] where the shells chosen for the negative parity band were $f_{5/2}$ and $p_{1/2}$. The RTRP calculations showed however that at deformation $\beta_2 \approx 0.37$ the $p_{3/2}$,$\Omega = 3/2$ state is preferred (Table 6b). Therefore the negative parity band was calculated here with the $p_{3/2}$ shell.

A crucial value to select the best theoretical reproduction of the experiment is the ratio of total transition probabilities

$$\lambda = \frac{T(\mathrm{E2}, I \to I-2)}{T(\mathrm{E2}, I \to I-1) + T(M1)} = \frac{\mathrm{Int.}_\gamma(I \to I-2)}{\mathrm{Int.}_\gamma(I \to I-1)}, \tag{6}$$

which can be compared with the ratio of the measured γ-intensities. When looking at $B(M1)$ values and mixing ratios δ one should keep in mind that variations between states of different signature depend on the triaxiality γ taken into account, the smaller the triaxiality the smaller the variations.

The positive parity band on the $g_{9/2}$ intruder state is reproduced by AROVM2 as well as by RTRP albeit the AROVM2 level energies are compressed due to a Coriolis

Table 6

Rotor model calculations: comparison between experimental and theoretical data for excitation energies and mixing ratios.

Comment: in case E2/M1 mixing ratios were determined only by angular distribution an exp. mixing ratio −0.6(4) was assumed, see Section 2.5. Legend: E_x = excitation energy (keV). λ = Int.$_\gamma(I \to I-2)$/Int.$_\gamma(I \to I-1)$, δ = E2/M1 mixing ratio, see Section 2.5, B(E2)= reduced E2 transition probabilities (e^2b^2), B(M1)= reduced M1 transition probabilities (μ_N^2).

(a) Comparison of rotor model calculations for positive parity band.

RTRP: $\beta \approx 0.37$, $\varepsilon_4 = 0.04$, $\gamma = 15°$, $E(2^+_{\text{core}}) = 224$ keV, Coriolis attenuation=0.5; the rotational band is built on: 85% $|4\,4\,9/2\,5/2\rangle$ + 6% $|4\,2\,5/2\,5/2\rangle$ + 4% $|4\,2\,5/2\,1/2\rangle$ with the quantum numbers $|N\,L\,J\,\Omega\rangle$.

AROVM2: $\beta = 0.37$, $\gamma = 15°$, $E(2^+_{\text{core}}) = 224$ keV, $E_{\text{Fermi}} - E(g_{9/2})_{\beta=0} = -3$ MeV, $E(d_{5/2})_{\beta=0} - E(g_{9/2})_{\beta=0} = 5$ MeV; chosen states: $g_{9/2}$ mixed with $d_{5/2}$

	Experiment				RTRP				AROVM2			
$2I$	E_x (keV)	λ	$\lvert\delta\rvert$	$B(E2, I \to I-2)$ $B(E2, I \to I-1)$ $B(M1, I \to I-1)$	E_x (keV)	λ	δ	$B(E2)_{\Delta I=2}$ $B(E2)_{\Delta I=1}$ $B(M1)$	E_x (keV)	λ	$\lvert\delta\rvert$	$B(E2)_{\Delta I=2}$ $B(E2)_{\Delta I=1}$ $B(M1)$
1	–				585				1293			
3	–				698				753			
5	0				0				0			
7	187		0.55(6)	–	210		−0.30	–	133		0.19	–
				2.68(28)				0.32				0.21
				0.13(2)				0.11				0.07
9	378	0.37(3)	0.56(7)	0.142(13)	460	0.5	−0.25	0.10	297	0.2	0.15	0.07
				2.78(51)				0.24				0.17
				0.23(2)				0.18				0.15
11	770	0.69(3)	0.6(4)	0.20(1)	791	1.2	−0.29	0.17	592	0.5	0.24	0.11
				0.55(53)				0.18				0.12
				0.16(6)				0.17				0.12
13	1067	2.84(16)	0.6(4)	0.20(1)	1104	2.0	−0.19	0.21	807	1.4	0.11	0.15
				1.3(12)				0.14				0.09
				0.22(8)				0.26				0.26
15	1594	1.4(1)	0.6(4)	>0.25(1)	1569	2.8	−0.32	0.24	1286	1.4	0.29	0.16
				>0.44(43)				0.10				0.06
				>0.24(9)				0.15				0.11

Table 6 — continued

	Experiment				RTRP				AROVM2			
$2I$	E_x (keV)	λ	$\lvert\delta\rvert$	$B(E2, I \to I-2)$ $B(E2, I \to I-1)$ $B(M1, I \to I-1)$	E_x (keV)	λ	δ	$B(E2)_{\Delta I=2}$ $B(E2)_{\Delta I=1}$ $B(M1)$	E_x (keV)	λ	$\lvert\delta\rvert$	$B(E2)_{\Delta I=2}$ $B(E2)_{\Delta I=1}$ $B(M1)$
17	1963	6.1(5)	0.6(4)	>0.134(6) >0.48(47) >0.13(5)	1927	4.9	−0.16	0.27 0.08 0.31	1497	6.2	0.07	0.19 0.05 0.35
19	2629	2.7(4)			2539	4.9	−0.37	0.28 0.07 0.13	2162	2.2	0.33	0.19 0.03 0.10
21	3049				2938	9.9	−0.14	0.31 0.06 0.35	2361	21	0.04	0.21 0.03 0.44

Table 6

Rotor model calculations: comparison between experimental and theoretical data for excitation energies and mixing ratios.

Comment: in case E2/M1 mixing ratios were determined only by angular distribution an exp. mixing ratio −0.6(4) was assumed, see Section 2.5. Legend: E_x = excitation energy (keV). $\lambda = \mathrm{Int.}_\gamma(I \to I-2)/\mathrm{Int.}_\gamma(I \to I-1)$, δ = E2/M1 mixing ratio, see Section 2.5, B(E2)= reduced E2 transition probabilities (e^2b^2), B(M1)= reduced M1 transition probabilities (μ_N^2).

(b) Comparison of rotor model calculations for negative parity band: $p_{3/2}+f_{5/2}$.

RTRP: $\beta \approx 0.37$, $\varepsilon_4 = 0.04$, $\gamma = 12°$, $E(2^+_{\mathrm{core}}) = 224$ keV, Coriolis attenuation=1.0; the rotational band is built on: 45% $|3\,1\,3/2\,3/2\rangle$ + 33% $|3\,3\,5/2\,3/2\rangle$ + 11% $|3\,1\,1/2\,1/2\rangle$ with the quantum numbers $|N\,L\,J\,\Omega\rangle$.

AROVM2: $\beta = 0.37$, $\gamma = 12°$, $E(2^+_{\mathrm{core}}) = 224$ keV, $E_{\mathrm{Fermi}} - E(f_{5/2})_{\beta=0} = 0.5$ MeV, $E(p_{3/2})_{\beta=0} - E(f_{5/2})_{\beta=0} = -0.8$ MeV; chosen states: $f_{5/2}$ mixed with $p_{3/2}$

	Experiment				RTRP				AROVM2			
$2I$	E_x (keV)	λ	$\lvert\delta\rvert$	$B(\mathrm{E2}, I \to I-2)$ $B(\mathrm{E2}, I \to I-1)$ $B(\mathrm{M1}, I \to I-1)$	E_x (keV)	λ	δ	$B(\mathrm{E2})_{\Delta I=2}$ $B(\mathrm{E2})_{\Delta I=1}$ $B(\mathrm{M1})$	E_x (keV)	λ	$\lvert\delta\rvert$	$B(\mathrm{E2})_{\Delta I=2}$ $B(\mathrm{E2})_{\Delta I=1}$ $B(\mathrm{M1})$
1					1036				573			
3	0				0				0			
5	179		0.6(2)	–	172		−0.20	–	116			–
				1.88(88)				0.33				0.21
				0.12(7)				0.16				0.03
7	432	0.36(2)	0.6(4)	0.17(1)	411	0.4	−0.20	0.14	401	2.0	3.0	0.09
				1.8(17)				0.20				0.10
				0.22(8)				0.20				0.008
9	726	0.92(5)	0.6(4)	0.27(6)	718	1.0	−0.20	0.20	624	9.2	1.4	0.15
				1.8(18)				0.13				0.09
				0.30(11)				0.22				0.03
11	1086	1.6(1)	0.6(4)	0.38(11)	1090	2.3	−0.21	0.24	1113	18	3.9	0.15
				1.3(12)				0.09				0.04
				0.32(11)				0.20				0.002
13	1467	2.0(2)	0.6(4)	0.25(8)	1525	3.4	−0.20	0.27	1287	63	0.8	0.19
				0.88(86)				0.07				0.04
				0.25(9)				0.22				0.05
15	1930	4.9(4)	0.6(4)	>0.26(1)	2029	6.2	−0.23	0.29	1887	28	11	0.19
				>0.29(28)				0.05				0.02
				>0.12(4)				0.17				10^{-6}

Table 6 — continued

	Experiment				RTRP				AROVM2			
$2I$	E_x (keV)	λ	$\|\delta\|$	$B(\mathrm{E2}, I \to I-2)$ $B(\mathrm{E2}, I \to I-1)$ $B(\mathrm{M1}, I \to I-1)$	E_x (keV)	λ	δ	$B(\mathrm{E2})_{\Delta I=2}$ $B(\mathrm{E2})_{\Delta I=1}$ $B(\mathrm{M1})$	E_x (keV)	λ	$\|\delta\|$	$B(\mathrm{E2})_{\Delta I=2}$ $B(\mathrm{E2})_{\Delta I=1}$ $B(\mathrm{M1})$
17	2383	7.3(13)			2579	7.5	−0.20	0.30 0.04 0.21	2126	557	0.5	0.21 0.02 0.06
19	2931				3216	13	−0.25	0.31 0.03 0.14	3047	24	1.5	0.20 0.01 0.003

interaction calculated program-inherently to large by an incomplete parameterization. On the other hand, the intensity ratios calculated by AROVM2 agree better.

The transition probabilities in the negative parity band cannot be reproduced by AROVM2 calculations at all. In AROVM2 calculations only two shell model states can be occupied by the single particle. But no combination of any two of the three shell model states near the Fermi surface ($f_{5/2}$, $p_{3/2}$ and $p_{1/2}$) is capable to reproduce the experiment as can be seen when comparing the intensity ratios. Other AROVM2 calculations confirm, that large M1 transition probabilities between negative parity levels are generated by transitions between the shells $p_{3/2}(j = L+1/2)$ and $p_{1/2}(j = L-1/2)$. In accordance, in RTRP calculations the $B(\mathrm{M1})$ values dropped if the $p_{1/2}$ state was excluded. As the RTRP calculations agree well with experiment when the $p_{1/2}$ state is taken into account, it has to be concluded: all mixing Nilsson states must be considered; but especially the $f_{5/2}$, $p_{3/2}$ and $p_{1/2}$ states are needed to describe the $K = 3/2$ negative parity band.

Now looking again at the sidebands, calculations were done trying to reproduce the yrare levels by triaxiality. These comparisons were done only with AROVM2, because RTRP solely calculates the yrast band. As mentioned before, the possible triaxiality is constricted by β^+-decay data of ^{75}Rb to less than 15° for negative parity and to less than 20° for positive parity [15,19]. Under these conditions no agreement could be found for the yrare band between experimental level energies combined with spins and AROVM2 calculations. In case of the $g_{9/2}$ sideband the strong signature splitting could not be reproduced, even if a calculated band-head spin of 5/2 is considered because of possibly ambiguous experimental spins. Although AROVM2 failed to reproduce the branching ratios in the negative parity band, it agrees in excitation energies and spin with the experiment. Therefore, also for the negative parity sideband triaxiality is deemed to be excluded because the unambiguous yrare band-head spin of 5/2 could not be reproduced. The yrare band-head spin was calculated by AROVM2 for all parameter sets equal to the yrast band-head spin.

3.3. Prolate–oblate mixing

3.3.1. Opposite deformation of favoured and unfavoured yrast band

In order to explain the measured large $Q_0(\Delta I = 1)/Q_0(\Delta I = 2)$ ratios we discussed in Ref. [19] prolate-oblate mixing. The predictions from our simple model can now be compared with experimental findings. The model assumed the yrast bands of opposite signature to be of opposite deformation: for example the favoured band to be predominantly prolate and the unfavoured to be predominantly oblate. Under these assumptions the following predictions could be made (see Ref. [19]): low spin sidebands should exist and the individual $B(\mathrm{E2})$ transition probabilities should be reduced compared to neighboring even–even nuclei, the $B(\mathrm{E2}, \Delta I = 2)$ values being more reduced than the $B(\mathrm{E2}, \Delta I = 1)$.

The sidebands have been found indeed with the OSIRIS_12 measurement. But only for negative parity this sideband starts at the predicted [19] spin $I + 1$ (I = yrast band-

head spin). The low spin negative parity level scheme would be reproduced very well by prolate-oblate mixing between a strongly coupled deformation aligned $K = 3/2$ band with $\beta_2 \approx +0.4$ and a weakly coupled rotational aligned $\alpha = 5/2$ band with $\beta_2 \approx -0.2$ ($\alpha \equiv$ quantum number for spin coupling to the rotational axis, $K \equiv$ quantum number for spin coupling to the deformation axis [54]). The second aspect of reduced $B(\mathrm{E2}, \Delta I = 2)$ values cannot be confirmed. On the contrary, the $B(\mathrm{E2}, \Delta I = 2)$ are somewhat larger than calculated. This fact is explainable by a larger prolate deformation. As for the experimental $B(\mathrm{E2}, \Delta I = 1)$ values, they depend crucially on the experimental mixing ratios. The mixing ratios unambiguously fixed by internal conversion electron measurement yield very large $B(\mathrm{E2}, \Delta I = 1)$ values in the low spin region of the $g_{9/2}$ band, which is calculated as originating from a pure [422]5/2 state. This feature is unexplainable, neither by pure prolate deformation nor by the prolate-oblate mixing model discussed here, unless assuming unreasonable large deformations.

3.3.2. Opposite deformation of yrast and yrare band

We now recall the TRS calculations of the cranking model (Fig. 11). There two potential energy minima were to be seen: an absolute minimum at large prolate deformation and a second minimum at somewhat less oblate deformation. The yrare band head energies are nicely reproduced by the energy offset of the oblate potential energy minimum compared to the prolate minimum. At $\hbar\omega = 0.2$ MeV, representing the first E2 transition, the energy offset is 800–900 keV for positive parity and 600–700 keV for negative parity. The experimental sideband-head energies are well in the error margins of about 140 keV for the calculated band-head energies. These error margins were determined by comparing theoretical and experimental band-head energies given in Ref. [1]. Moreover, since the $B(\mathrm{E2}, \Delta I = 2)$ and the yrast level energies can be reproduced very well by rotor model calculations using large prolate deformation, we regard the yrast bands of either parity to be generated by a prolate deformed core.

There are further fingerprints from experiment, which induce us to regard the 1qp yrare bands as originated from oblate deformation. The loss of pairing correlations at comparatively low $\hbar\omega$ in the negative parity sideband can be explained if oblate deformation is assumed. In case of the $9/2^+$ yrare band we even have an experimental hint for oblate deformation: in the isotone ^{73}Se the $9/2^+$ ground-state band exhibits the same pattern of a strong signature splitting. Here the mixing ratio of the first $\Delta I = 1$ transition has been determined revealing a positive sign, from which an oblate deformation for the low spin levels has been infered [59]. Thus, we now consider the low spin level scheme to be dominated by prolate-oblate shape coexistence.

Positive parity

The yrast band is interpreted as to be generated from a rather pure [422]5/2 state at large prolate deformation. The sideband on the $9/2^+$ state with a very large signature splitting must be a Coriolis interaction disturbed band, generated either by a low Ω $g_{9/2}$ single particle state or a weakly deformed $\Omega = 9/2$. Looking into a Nilsson scheme [1]

we find above the magic nucleon number for small oblate deformation $Z, N = 34$ at $\beta_2 \approx -0.18$ three crossing Nilsson states: the [310]1/2 and the [301]3/2 of the $f_{5/2}$ state and the [404]9/2, which can explain the $9/2^+$ yrare band head and agrees with the prolate-oblate shape coexistence point of view. The [413]7/2 found at larger oblate deformation $\beta_2 \approx -0.26$ would lead to a $7/2^+$ band-head spin, which was excluded by DCO ratios. The other possibility of a [440]1/2 state with a small prolate deformation, rotational aligned by a strong Coriolis interaction resulting in an $\alpha = 9/2$ band head spin, cannot be altogether dismissed. But this configuration should mix strongly with the [422]5/2 and is moreover not supported by the TRS calculations. These not only show a second minimum at oblate deformation but this minimum in fact disappears at $\hbar\omega \approx 0.5$ MeV. This agrees very well with the highest rotational energies detected in the sidebands (1051 and 1095 keV). All these arguments together induce us to interpret the positive parity 1qp yrare band as to be effected by a small oblate deformation $\beta_2 \approx -0.2$. The observed transition probabilities further strengthen our conviction. The intra-band $\Delta I = 1$ transitions $\{15/2_2\} \rightarrow 13/2_2$ and $\{11/2_2\} \rightarrow 9/2_2$ are energetically favoured compared to the inter-band $\Delta I = 0$ transitions $\{15/2_2\} \rightarrow 15/2_1$ and $\{11/2_2\} \rightarrow 11/2_1$ if both have to occur through an E2/M1 transition. But, the intra-band transitions were not found. Thus, the $\Delta I = 0$ inter-band transitions have to have a relatively strong E0 transition probability indicating a shape change [60,61].

Negative parity

When discussing the negative parity 1qp yrare band the 3qp-sideband has to be taken into account, because this band decays with a strong branch (844_{side} keV, $17/2_2^-$ (2957 keV) $\rightarrow 13/2_2^-$ (2113 keV)) into the 1qp-sideband. Surprisingly the 3qp signature partners show very different inter-band connections as discussed in the next to last paragraph of Section 3.1. Neither the positive signature yrast nor the negative signature 1qp yrare are connected to the 3qp-sideband although those transitions are as favoured by energy as are the observed connections. This feature would be explained by a prolate-oblate mixing as discussed in Section 3.3.1 and Ref. [19]: a prolate 3qp-sideband would decay only into predominantly prolate levels while the predominantly oblate band would not be connected to unmixed prolate high spin levels. But as mentioned in Section 3.3.1, the $B(\text{E2}, \Delta I = 2)$ values are not reduced in the 1qp yrast band.

The possibility, that the negative signature 1qp band on the $7/2^-$ belongs to another structure, separate from both yrast and oblate positive signature 1qp band on the $5/2^-$, can be excluded as long as a population of an unseen $3/2^-$ band-head level has not been proved. A [303]7/2 band can be excluded, because this Nilsson state reaches the Fermi level only at deformations $\beta_2 > 0.6$. Thus, the resulting band structure should evolve a strong coupling scheme. In this mass region the maximum negative parity single particle spin reachable is $\Omega = 5/2$ of the $f_{5/2}$ state, from which the 1qp-sideband must be generated.

We now study the possibility that both 1qp-sidebands belong to the same oblate structure. Comparing the transition probabilities ($\propto E_\gamma^3$), the 1qp intra-band transitions

are more than 10 times less probable than the $\Delta I = 1$ inter-band transitions, which might explain the unconnected signature partners in the yrare band. Although a prolate deformed 1qp-sideband cannot be excluded, this was dismissed because of the quite different decay paths of the 3qp-sideband.

For the sake of simplicity we consider the 1qp-sideband to be a weakly coupled, rotational aligned $[310]1/2$, $\alpha = 5/2$ band of oblate deformation, although we expect the 1qp yrare band to be as mixed as the yrast band. To explain the different decay paths of the 3qp-sideband one could suppose the 3qp-sideband to be prolate-oblate mixed. But, in the whole neutron deficient mass region $A \approx 70-80$ no oblate deformation has been found above the first pair alignment.

Remember now the reduced alignment frequency (Fig. 13, bottom), which was interpreted as to be due to a $g_{9/2}$ neutron pair alignment at oblate deformation. By these aligned neutrons ^{75}Kr is driven to prolate deformation. Therefore, a change from oblate to prolate deformation, maybe via triaxiality, in the lowest three levels of the 3qp-sideband could be the source of the the quite different decay paths. The 844_{side} keV transition marks the neutron pair alignment, the 927 keV transition continues the oblate 1qp-sideband. As soon as the the nucleus reaches prolate deformation, the 1019 keV transition into the prolate yrast band is strongly favoured.

In conclusion, in case of the negative parity bands no definite description of the prolate-oblate shape coexistence can be given. Nevertheless, all three descriptions demand two states of opposite deformation $\beta_2 \approx +0.4$ and $\beta_2 \approx -0.2$.

All in all the experimental facts are best reproduced by the third interpretation of a predominantly prolate 1qp yrast band and a predominantly oblate 1qp yrare band with a transition from oblate to prolate deformation in the lowest levels of the 3qp-sideband.

4. Summary

The present investigation showed the strong influence of both the single particle gaps at $Z, N = 36$ and $Z, N = 38$ on the structure of ^{75}Kr. This can be deduced from the single particle configurations of the experimental band heads and the deformations determined from lifetimes. The neutrons prefer prolate and the protons favor oblate deformation. The pn-interaction might be the origin of the drive to large quadrupole deformation, which is even more enhanced and stabilized by the single neutron above the $N = 38$ shell gap at $\beta_2 \approx +0.4$.

The lifetimes measured in coincidence yield very large deformations ($\beta_2 \approx 0.4-0.5$ depending on the model used) for the yrast bands. The lifetimes in the yrare bands could not be determined because of insufficient statistics.

The alignment frequencies hint at different structures of the yrare and the yrast bands of either parity. The positive parity 1qp yrare band is not observed above $\hbar\omega \approx 0.6$ MeV, while the yrast band continues up to spin 45/2. The yrast bands of both parities show a large upbending up to $6\hbar$ beginning at $\hbar\omega \approx 0.6$ MeV. A part of this gain is explained for both parities by cranking calculations as an aligning $g_{9/2}$ proton pair at large prolate

deformation. The positive signature partner of the negative parity yrast band is not observed after this first alignment, while in the negative signature partner of the negative parity yrast band the $g_{9/2}$ neutron pair aligns simultaneously with the $g_{9/2}$ proton pair at $\hbar\omega \approx 0.6$ MeV in accordance with the interpretation of neighboring nuclei (^{74,76}Kr, ^{75}Br). In the positive parity yrast band the $g_{9/2}$ neutron pair alignment is blocked up to $\hbar\omega \approx 0.8$ MeV,

The $g_{9/2}$ 1qp-bands have band-head spins of 5/2 (1qp yrast) and 9/2 (1qp yrare), respectively. The positive parity 1qp yrast band is explained by both the rotor model calculations RTRP and AROVM2 as a rotational band on the [422]5/2 Nilsson state. The deviations between the RTRP and AROVM2 calculations for the negative parity band show: the negative parity 1qp yrast band is built on a band-head configuration strongly mixed from $f_{5/2}$, $p_{3/2}$ and $p_{1/2}$ with band-head spin 3/2. Probably, the 1qp yrare band with band-head spin 5/2 is mixed as well.

For the 1qp yrast bands of either parity the band-head spins, $B(\mathrm{E2}, \Delta I = 2)$ and $B(\mathrm{M1})$ transition probabilities can be reproduced by the RTRP rotor calculation using a large prolate deformation. But, the experimental mixing ratios determined by conversion electron measurement and the resulting $B(\mathrm{E2}, \Delta I = 1)$ transition probabilities are more enhanced than expected for a prolate deformed nucleus. Additionally, the 1qp yrare bands cannot be explained by triaxiality, and for the positive parity 1qp yrare band favoured $\Delta I = 0$ transitions between yrare and yrast band hint at a shape change.

Although for numerous yrast band $\Delta I = 1$ transitions the angular distribution measurement yielded mixing ratios $\delta \approx -1$, there remain some doubts on the accuracy of the DSA-affected angular distributions. Therefore, up to now only the E2/M1-mixing ratios $\delta(187\ \mathrm{keV}) = -0.55(6)$ and $\delta(191\ \mathrm{keV}) = -0.56(7)$ have been fixed unambiguously. For the 179_2 keV transition a mixing ratio $\delta = \pm 0.6(2)$ was adopted. The resulting exceptionally large $B(\mathrm{E2}, \Delta I = 1)$ transition probabilities in the low spin region are interpreted for either parity to be due to prolate-oblate mixing between a prolate yrast and an oblate yrare 1qp band. Further investigations of high precision are needed to elucidate this subject.

The negative parity 1qp-sideband shows a pair alignment already at $\hbar\omega \approx 0.4$–0.5 MeV, which can be interpreted by cranking calculations as aligning $g_{9/2}$ neutrons at smaller oblate deformation. The prolate shape is energetically favoured and the oblate can be maintained only until the first alignment. The experimental data agree well with cranking model calculations although the calculated values of deformation and pair alignment frequency for the yrast bands are about 10% to small compared to the experiment. This deviation might be due to the pn-interactions not incorporated in the CSM calculations.

Because of all these experimental facts together and the good agreement with cranking model calculations, the 1qp yrare bands are interpreted to originate from small oblate deformation (positive parity: [404]9/2, $\beta_2 \approx -0.2$; negative parity: [301]1/2 rotational aligned to $\alpha = 5/2$, $\beta_2 \approx -0.2$). Thus, for the first time a prolate-oblate shape coexistence has been found in the extended level scheme of ^{75}Kr.

Acknowledgements

We gratefully acknowledge the useful discussions with J.L. Wood. We thank G. Böhm, A. Dewald and R. Reinhardt for their help during the installation of plunger and Mini Orange systems. This research was supported by the German Federal Ministry of Research and Technology under contracts No. 06OK143 and 06OK668.

References

[1] W. Nazarewicz, J.Dudek, R. Bengtsson, T. Bengtsson, and I. Ragnarsson, Nucl. Phys. A 435 (1985) 397.
[2] K. Heyde, J. Jolie, J. Moreau, J. Ryckebusch, M. Waroquier, P. van Duppen, M. Huyse and J.L. Wood, Nucl. Phys. A 466 (1987) 189.
[3] K. Heyde, J. Ryckebusch, M. Waroquier and J.L. Wood, Nucl. Phys. A 484 (1988) 275.
[4] J.H. Hamilton, A.V. Ramayya, W.T. Pinkston, R.M. Ronningen, G. Garcia-Bermudez, H.K. Carter, R.L. Robinson, H.J. Kim and R.O. Sayer, Phys. Rev. Lett. 32 (1974) 239.
[5] R. Bengtsson, P. Möller, J.R. Nix and J. Zhang, Phys. Scri. 29 (1984) 402.
[6] M. Wiosna, J. Busch, J. Eberth, M. Liebchen, T. Mylaeus, N. Schmal, R. Sefzig, S. Skoda and W. Teichert, Phys. Lett. B 200 (1988) 255.
[7] T. Mylaeus, J. Busch, J. Eberth, M. Liebchen, R. Sefzig, S. Skoda, W. Teichert, M. Wiosna, P. von Brentano, K. Schiffer, K.O. Zell, A.V. Ramayya, K.H. Maier, H. Grawe, A. Kluge and W. Nazarewicz, J. Phys. G 15 (1989) L135.
[8] R.B. Piercey, J.H. Hamilton, R. Soundranayagam, A.V. Ramayya, C.F. Maguire, X.-J. Sun, Z.Z. Zhao, R.L. Robinson, H.J. Kim, S. Frauendorf, J. Döring, L. Funke, G. Winter, J. Roth, L. Cleemann, J. Eberth, W. Neumann, J.C. Wells, J. Lin, A.C. Rester and H.K. Carter, Phys. Rev. Lett. 47 (1981) 1514.
[9] R.B.Piercey, A.V.Ramayya, J.H. Hamilton, X.J. Sun, Z.Z. Zhao, R.L. Robinson, H.J. Kim and J.C. Wells, Phys. Rev. C 25 (1982) 1941.
[10] J. Heese, D.J. Blumenthal, A.A. Chishti, P. Chowdurry, B. Crowell, P.J. Ennis and Ch. Winter, Phys. Rev. C 43 (1991) R921.
[11] S. Freund, J. Altmann, F. Becker, T. Burkardt, J. Eberth, L. Funke, H. Grawe, J. Heese, U. Hermkens, H. Kluge, K.-H. Maier, T. Mylaeus, H. Prade, S. Skoda, W. Teichert, H.-G. Thomas, A. v.d. Werth, and G. Winter, Phys. Lett. B 302 (1993) 167.
[12] C. Miehé, Ph. Dessagne, Ch. Pujol, G. Walter, B. Jonson, M. Lindroos and the ISOLDE Collaboration, CRN report 94-22.
[13] G. Winter, J. Döring, W.D. Fromm, L. Funke, P. Kemnitz and E. Will, Z. Phys. A 309 (1983) 243.
[14] G. Garcia Bermudez, C. Baktash and C.J. Lister, Phys. Rev. C 30 (1984) 1208.
[15] M.A. Herath-Banda, A.V. Ramayya, L. Cleemann, J. Eberth, J. Roth, T. Heck, N. Schmal, T. Mylaeus, W. Koenig, B. Martin, K. Bethge and G.A. Leander, J. Phys. G 13 (1987) 43.
[16] A.A. Chishti, W. Gelletly, C.J. Lister, J.H. McNeill, B.J. Varley, D.J.G. Love and O. Skeppstedt, Nucl. Phys. A 501 (1989) 568.
[17] D.F. Winchell, M.S. Kaplan, J.X. Saladin, H. Takai, J.J. Kolata and J. Dudek, Phys. Rev. C 40 (1989) 2672.
[18] M.A. Cardona, G. Garcia-Bermudez, A. Filevich and E. Achterberg, Phys. Rev. C 42 (1990) 591.
[19] S. Skoda, J.L. Wood, J. Eberth, J. Busch, M. Liebchen, T. Mylaeus, N. Schmal, R. Sefzig, W. Teichert and M. Wiosna, Z. Phys. A 336 (1990) 391.
[20] K.O. Zell, Nucl. Instr. and Meth. A 236 (1985) 655.
[21] H.Hanewinkel, Diploma thesis, Universität Köln 1981, unpublished;
S. Albers, A. Clauberg, A. Dewald, C. Wesselborg and A. Zilges, Verh. DPG 6/1988, p. 227;
program LEONE for the determination of γ intensities;
S. Skoda, program EFF for efficiency correction, Universität zu Köln, unpublished;
N. Schmal, program FITPOL for the determination of angular distribution coefficients, Universität zu Köln, unpublished;

W. Krips, program BFIT for the determination of electron intensities, Universität zu Köln, unpublished;
H. Wolters, program TRIXI for the $\gamma\gamma$ analysis, Universität zu Köln, unpublished;
I. Wiedenhöver, program TOPFIT to fit various curves and determine their parameters, Universität zu Köln, unpublished;
F. Seiffert, program APATHIE to fit various curves and determine their parameters, Universität zu Köln, unpublished;
G. Böhm, programs LEBEN4 and APALEBEN to determine lifetimes, Universität zu Köln, unpublished.
[22] D. Weil, R. Wirowski, E. Ott, A. Dewald, P. von Brentano, H. Wolters and R.M. Lieder, Nucl. Phys. A 567 (1994) 431;
Program XPLO for the determination of angular distribution coefficients.
[23] U. Neuneyer, A. Mertens, R. Kühn, I. Wiedenhöver, O. Vogel, M. Wilhelm, M. Luig, K.O. Zell, A. Gelberg, P. von Brentano and T. Otsuka, Nucl. Phys. A 607 (1996) 299;
Program CORREL to calculate directional correlations.
[24] R.M. Lieder, H. Jäger, A. Neskakis, T. Venkova and C. Michel, Nucl. Instr. and Meth. 220 (1984) 363.
[25] S. Skoda, Diploma Thesis, Universität zu Köln 1987, unpublished.
[26] V. Zobel, L. Cleemann, J. Eberth, H.P. Hellmeister, W. Neumann, and N. Wiehl, Nucl. Instr. and Meth. 171 (1980) 223.
[27] J. Heese, N. Martin, C.J. Gross, W. Fieber, K.P. Lieb, A. Kuhnert, K.H. Maier and X. Sun, Phys. Rev. C 41 (1990) 1553.
[28] J. van Klinken, S.J. Feenstra, K. Wisshak and H. Faust, Nucl. Instr. and Meth. 130 (1978) 427.
[29] J.H. Hamilton, *in* The electromagnetic interaction in nuclear spectroscopy, ed. W.D. Hamilton (North-Holland, Amsterdam, 1975).
[30] K. Alder and A. Winther, Coulomb Excitation, A Collection of Reprints (Academic Press, New York, 1966).
[31] J. Bea, Ph.D. Thesis and to be published.
[32] M. Keim, A. Arnold, W. Borchers, U. Georg, A. Klein, R. Neugart, L. Vermeeren, R.E. Silverans and P. Lievens, Nucl. Phys. A 586 (1995) 219.
[33] A. Dewald, P. Sala, R. Wrzal, G. Böhm, D. Lieberz, G. Siems, R. Wirowski, K.O. Zell, A. Gelberg, P. v. Brentano, P. Nolan, A.J. Kirwan, P.J. Bishop, R. Julin, A. Lampinen and J. Hattula, Nucl. Phys. A 545 (1992) 822.
[34] J. Altmann, A. Dewald, K.O. Zell and P. v. Brentano, Nucl. Instr. and Meth. A 321 (1992) 59.
[35] A. Dewald, S. Harrissopulos and P. v. Brentano, Z. Phys. A 334 (1989) 163.
[36] G. Böhm, A. Dewald, P. Petkov and P. v. Brentano, Nucl. Instr. and Meth. A 329 (1993) 248.
[37] J. Heese, K.P. Lieb, L. Lühmann, S. Ulbig, B. Wörmann, D. Alber, H. Grawe, H. Haas and B. Spellmeyer, Phys. Rev. C 36 (1987) 2409.
[38] L. Lühmann, M. Debray, K.P. Lieb, W. Nazarewicz and B. Wörmann, Phys. Rev. C 31 (1985) 828;
L. Lühmann, Ph.D. Thesis, unpublished.
[39] J. Heese, K.P. Lieb, L. Lühmann, F. Raether, B. Wörmann, D. Alber, H. Grawe, J. Eberth and T. Mylaeus, Z. Phys. A 325 (1986) 45.
[40] V.G. Kiptilyi, I.K. Lemberg, A.S. Mishin and A.A. Pasternak, Bull. Acad. Sci. USSR, Phys. Ser. 43 (1979) 26.
[41] H.P. Hellmeister, E. Schmidt, M. Uhrmacher, R. Rascher, K.P. Lieb and D. Pantelica, Phys. Rev. C 17 (1978) 2113.
[42] J.H. Hamilton, H.L. Crowell, R.L. Robinson, A.V. Ramayya, W.E. Collins, R.M. Ronningen, V. Maruhn-Rezwani, J.A. Maruhn, N.C. Singhal, H.J. Kim, R.O. Sayer, T. Magee and L.C. Whitlock, Phys. Rev. Lett. 36 (1976) 340.
[43] K.E.G. Löbner, G. Dannhäuser, D.J. Donahue, O. Häussler, R.L. Hershberger, R. Lutter, W. Klinger and W. Witthuhn, Z. Phys. A 274 (1975) 251.
[44] B. Wörmann, K.P. Lieb, R. Diller, L. Lühmann, L. Cleemann and J. Eberth, Nucl. Phys. A 431 (1984) 170.
[45] G. Winter, private communication, cited from Ref. [44].
[46] J. Keinonen, K.P. Lieb, H.P. Hellmeister, A. Bockisch and A. Emling, Nucl. Phys. A 376 (1982) 246.
[47] E. Nolte, Y. Shida, Y.W. Kutschera, R. Prestele and H. Morinaga, Z. Phys. A 268 (1974) 267.
[48] C.J. Gross, J. Heese, K.P. Lieb, S. Ulbig, W. Nazarewicz, C.J. Lister, B.J. Varley, J. Billowes, A.A. Chishti, J.H. McNeill and W. Gelletly, Nucl. Phys. A 501 (1989) 367.
[49] A. Bohr and B.R. Mottelson, Nuclear Structure, vol. 2 (Benjamin, New York, 1975).

[50] C.J. Gross, J. Heese, K.P. Lieb, L. Lühmann, B. Wörmann, A.A. Chishti, W. Gelletly, C.J. Lister, J.H. McNeill and B.J. Varley, Z. Phys. A 331 (1988) 361.
[51] N. Martin, C.J. Gross, J. Heese and K.P. Lieb, J. Phys. G 15 (1989) L123.
[52] S.L. Tabor and J. Döring, Phys. Scri. T 56 (1995) 175.
[53] S.E. Larson, G. Leander and I. Ragnarsson, Nucl. Phys. A 307 (1978) 189.
[54] P. Ring and P. Schuck, The nuclear many-body problem (Springer, New York, 1980).
[55] H. Toki and A. Faessler, Nucl. Phys. A 253 (1975) 231.
[56] A. Faessler and H. Toki, Phys. Lett. B 59 (1975) 211.
[57] H. Toki and A. Faessler, Z. Phys. A 276 (1976) 35.
[58] H. Toki and A. Faessler, Phys. Lett. B 63 (1976) 121.
[59] F. Seiffert, R. Schwengner, L. Funke, W. Lieberz, R. Reinhardt, K.P. Schmittgen, D. Weil, G. Winter, R. Wrzal, K.O. Zell and P. v. Brentano, Z. Phys. A 340 (1991) 141.
[60] H. Morinaga and T. Yamazaki, In-beam Gamma-ray Spectroscopy (North-Holland, Amsterdam, 1976).
[61] J. Wood, Proc. Int. Conf. on nuclear shapes and nuclear structures at low excitation energies, Antibes, June 20–25, 1994, ed. M. Vergnes, D. Goutte, P.H. Heenen, J. Sauvage (Editions Frontières, Gif-sur-Yvette, 1994) p. 295.